Aus dem Zentrum für Medizinische Forschung
der Medizinischen Fakultät Mannheim
Direktor: Prof. Dr. med. Norbert Gretz
(Aufgelöst zum 16.04.2020)

Implementation of Tissue Clearing Protocols for Ex-vivo Analysis of Renal Tissue

Inauguraldissertation
zur Erlangung des Doctor scientiarum humanarum (Dr. sc. hum.)
der
Medizinischen Fakultät Mannheim
der Ruprecht-Karls-Universität
zu
Heidelberg

vorgelegt von
Tiziana Picascia

aus
Neapel
2023

Dekan: Prof. Dr. med. Sergij Goerdt
Referent: Prof. Dr. rer. nat. Benito Yard

TABLE OF CONTENTS

ABBREVIATIONS

(i)DISCO	(Immunolabeling-enabled)-3D Imaging of Solvent-Cleared Organs
3D	Three-dimensional
AHS	Amplifying Hydrogel Solution
AU	Airy Unit
CLARITY	Clear Lipid-exchanged Acrylamide-hybridized Rigid Imaging/ Immunostaining/ in situ hybridization–compatible Tissue hYdrogel
CM	Confocal microscopy
CNN	Convoluted Neural Network
CT	Computed tomography
CUBIC	Clear Unobstructed Brain/Body Imaging cocktails and Computational analysis
DMSO	Dimethyl sulfoxide
DOL	Degree of Labelling
ECi	Ethyl-cinnamate
ExM	Expansion microscopy
ExPath	Expansion Pathology
FP	Fluorescent Protein
GAGs	Glycosaminoglycans
GFP	Green Fluorescent Protein
HA	Hyaluronic Acid
Has2	hyaluronan synthase 2
IB4	Isolectin B4
IHC	Immunohistochemistry
KO	Knock out
LEA	Lycopersicon Esculentum Agglutinin

LSFM	Light-sheet fluorescence microscopy
NA	Numerical aperture
NIR	Near Infrared
NPH	Nephronophthisis
OTC	Optical tissue clearing
PBS	Phosphate Buffered Saline
PBST	Phosphate Buffered Saline with 0.5% Tween
PEI	Polyethylenimine
PFA	Paraformaldehyde
RI	Refractive index
ROI	Region of interest
RT	Room Temperature
SA	Sodium Acrylate
SNR	Signal-to-noise ratio
SRM	Super Resolution Microscopy
STED	Stimulated Emission Depletion
WGA	Wheat germ agglutinin
WS	Water-soluble
ZOOM	Zoom by hydrOgel cOnversion Microscopy

1 INTRODUCTION

While classical histology has evolved as a golden standard for morphological analysis of healthy and diseased tissues, spatial relationships and complexity of biological structures extending in multiple directions[1] are poorly captured by 2D visualization. To overcome these limitations, three-dimensional (3D) imaging and optical tissue clearing (OTC) techniques have emerged as promising alternatives. Moreover, OTC allows whole-organ imaging, circumventing the bias that may arise when selected histological sections are not representative of the entire organ. Over the last decades, tissue clearing in combination with state-of-the-art microscopy has been employed in a large number of studies on renal physiology and pathophysiology that addressed vascular and renal diseases[2]. The introduction of rapid clearing techniques and the use of light-sheet microscopy have already significantly contributed to kidney research and allowed the quantification of the glomerular number in murine kidneys[3]. Although whole-mount imaging provides robust and unbiased morphological information, it cannot be used for resolving biological nanostructures. To serve this purpose, Expansion Microscopy (ExM) has been developed recently for visualization and reconstruction of fine details in tissues. As such, ExM has been used for analysing the glomerular filtration barrier and resolving podocyte foot processes, which previously was only possible by electron microscopy[4, 5]. Even though 3D imaging and OTC techniques have matured and despite the large amount of currently available OTC protocols, the main hurdles for a more widely use of these techniques in research are processing time and costs. Hence, the development of more time-efficient and less costly methods or strategies for staining and handling big data generated by 3D imaging is still warranted.

1.1 OTC methods and kidney research

The main principle of OTC is to make tissues optically transparent that allows 3D reconstruction of these tissues by microscopy. OTC includes a broad set of techniques that renders samples transparent through the reduction of light scattering. The phenomenon of light scattering limits the absorption of light and is due to a mismatch of refractive index (RI) inside the tissue. Thus, intrinsic tissue inhomogeneities cause multiple scattering in biological material[6].

Since the seminal method description by Spalteholz a century ago[7], a large number of OTC protocols have been developed and are currently applied to analyse biological structures in a 3D manner. Currently, used clearing methods can be categorized into three groups, i.e. organic solvent-based tissue clearing, aqueous-based tissue clearing, and hydrogel embedding tissue clearing (Figure 1.1).

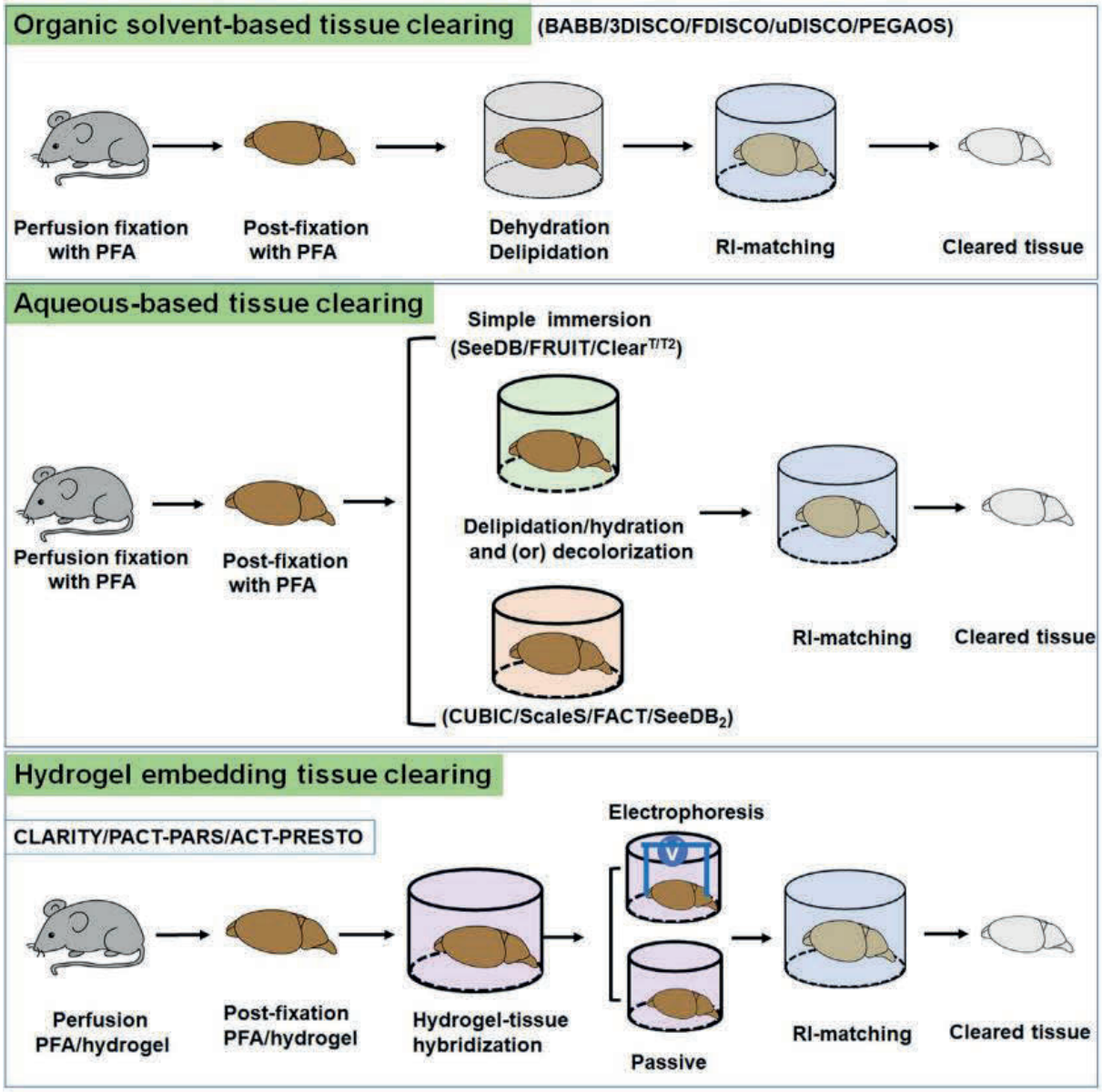

Figure 1.1 Schematic representation of tissue clearing categories adapted from Tian et al.[1]

Although organic solvents are usually toxic reagents and present several drawbacks, they have high RI and allow to achieve high transparency rapidly by lipid removal. However, prior to delipidation, tissue dehydration is required which may cause tissue shrinkage and fluorescence quenching. Instead, aqueous-based techniques are more user-friendly, safe, and in general preserve the endogenous fluorescence better [8]. The

latter is based on simple immersion or delipidation/hyper-hydration. Simple immersion consists of incubating the samples in reagents with high RI, resulting in low clearing efficacy, especially in intact organs. In this case, higher transparency can be achieved by using detergents and amino-alcohols that also aid in lipid removal. In addition, the use of rehydration agents, such as urea, increases tissue permeability by creating osmotic pressure within the tissue[9]. The use of the aforementioned reagents is implemented in the Clear unobstructed brain/body imaging cocktails and computational analysis (CUBIC) method, which utilizes a hyper-hydration urea-based mechanism as well as a high RI sucrose solution and very high levels of detergents[10]. Nevertheless, in comparison to organic solvent-based protocols, aqueous-based techniques are more time consuming.

Similar as for the aqueous-based techniques, also hydrogel embedding methods are based on the use of high concentrations of detergents. Gel-embedding has the advantage that it better protects the tissue from harsh treatments such as heat and electrophoresis[11], as is used in the Clear Lipid-exchange Acrylamide hybridized Rigid imaging in situ hybridization-compatible Tissue Hydrogel (CLARITY) protocol. Apart from this, tissue-gel hybrids perform well in maintaining the integrity of histological samples[12]. This method is amongst others employed in OTC techniques, such as ExM. The latter establishes clearing by digestion or denaturation and aims to physically expand the tissue, by embedding it in a swellable polymeric hydrogel.

Over the last years, the application of these techniques on renal biopsies has increased our understanding of kidney structure and function by providing more accurate and precise morphological information. As such, the CUBIC technique made it possible to visualize and quantify different renal structures in the whole kidney, e.g. morphology of the distal convoluted tubule[13], lymphatics[14], and sympathetic innervation[15,16]. OTC has also been employed to study dynamic processes such as protein uptake through a combination of intravital microscopy and CLARITY. This allowed us to investigate and quantify ligand uptake in the kidney in a spatial manner[17].

Among the broad range of OTC techniques, ethyl-cinnamate (ECi) can clear the kidney rapidly with high efficiency. However, when fluorescent reporters, e.g. green fluorescent protein (GFP), are present in the tissue, the main drawback of ECi is the loss of fluorescence due to quenching during the solvent-based clearing. Alternatively, its use in combination with immunolabeling and perfusion staining strategies has been adopted to detect proliferating cells in the tubulointerstitium[18] and to quantify the

number of glomeruli in a model of nephrotoxic nephritis[3]. Recently, a faster ECi protocol was used to evaluate glomerular size and dilation of the afferent arteriole as indirect estimations of increased intraglomerular pressure in diabetic nephropathy[19].
Given the wide variety of OTC methods, the optimal protocol to use can be selected based on several parameters such as tissue type, sample size, labelling strategy, and available equipment for optical imaging as reviewed by Avilov et al.[20]. Thus, the decolorizing action of amino alcohols is needed for heme-rich tissues like the liver or spleen[21], while soft tissues like lung and brains are cleared by most of the protocols. Despite the pros of using non-toxic reagents for processing tissue by aqueous and hydrogel-based techniques, large samples are preferably cleared by organic solvents. These reagents can rapidly clear whole organs according to simple procedures with demonstrated high-clearing performance and might as well facilitate imaging due to tissue shrinkage, which often occurs when using organic solvents.

1.2 Biological labelling in cleared tissue

Staining of structures and/or molecules and the selection of an appropriate fluorescent probe is of key importance in developing a suitable OTC method. Labelling strategies can be categorized as follows: 1) use of transgenic animals that are expressing gene-encoded biological probes, 2) use of a compatible immunohistochemistry (IHC) protocol, 3) perfusion or injection of fluorescent markers.
The use of fluorescent reporters is challenging, not only because of the risk of losing the fluorescence signal as a consequence of quenching but also because of high background fluorescence, which may result in a low signal-to-noise (SNR) ratio and thus making detection of a specific signal a tedious endeavour. Fluorescence quenching may occur because of high temperatures, harsh conditions, and corrosive reagents to which the samples are subjected to. To limit quenching in organic solvent-based OTC, the use of ethanol for dehydration can be replaced by other alcohols that better preserve the fluorescence signal of fluorescent protein (FP) as observed in second-generation ECi clearing (2ECi)[22]. Degradation of FP is mostly associated with oxidation of the FP and it may therefore be prevented by the use of antioxidants in the protocol[23]. Even when OTC protocols are suitable for imaging FP, intrinsic features of the FPs, e.g. low photo-stability, reduced brightness as well as a low expression level, may limit the success of this approach. In this regard, Kirschnick et al. recently

described a method for the evaluation of FPs fluorescent retention adaptable to different tissue clearing protocols[24].

IHC protocols as labelling strategy mostly make use of antibody staining. Although antibody staining works well in the majority of available OTC protocols, the pitfalls are that it is cost- and time-intensive when whole organ labelling is performed. It should also be emphasized that prior antibody testing is needed to ensure that the epitope is preserved after tissue processing. For whole organ staining, nanobodies that can easily diffuse throughout the tissue[25], stochastic electrotransport[26], or hydrodynamic pressure[27] can be used to enhance antibody penetration.

Perfusion or injection of fluorescent markers as labelling strategy have been successfully applied in a number of studies[28, 29]. It can be achieved by tissue immersion in stains, e.g. eosin, Congo Red, Picro Sirius red, Congo red or fluorescent Nissl, and can be used in combination with several OTC protocols[30]. Likewise, nuclear staining (DAPI/ HOECHST) has been successfully conducted in heart[28] and brain tissue[29] by sample immersion. More recently studies have been performed in which fluorescent molecules are injected or used in animal perfusion[31]. This seems to reduce costs and OTC processing time drastically for whole organs and is particularly well-suited for labelling the vasculature as will be addressed in the next paragraph.

1.3 3D imaging of vascular networks

The complexity of vascular networks can be assessed by sophisticated imaging modalities such as micro-computed tomography (CT), which can depict the spatial distribution of vessels at the capillary level. Although micro-CT can visualize the renal vascular structures in a 3D manner and thus can assess the spatial density of micro-vessels and vessel size[32], small-sized blood vessels with a diameter smaller than 10 µm, cannot be identified with accuracy[33].

Progress in OTC as well as in data acquiring at high resolution and at high speed have opened new avenues for 3D histological analysis of complex vascular architectures. Labelling of the vasculature can be achieved by the use of endothelial-specific antibodies or by expression of genetically encoded fluorescent proteins in endothelial cells. Anyhow, these approaches exhibit some technical limitations when combined with OTC, such as poor antibody penetration and fluorescence quenching as discussed in the previous paragraph. New fluorescent dyes for tracking vessels and capillaries have been developed and offer the opportunity to stain multiple organs

when injected intravenously. Examples hereof are fluorescent vessel-filling solutions, e.g. such as India Ink[34] and fluorescence-conjugated dextran[35]. Yet some of these dyes do not bind the endothelium and therefore may give rise to incomplete labelling of the vasculature. An alternative approach is the use of polymerizable solutions that contain the fluorescent tracer and form a stable gel inside the vessel lumen[36, 37]. Over the last years, different studies have focused on markers that can bind the endothelium specifically and can therefore label the vessels more reliably. Based on their lipophilic nature, carbocyanine dyes such as DiI and its substitutes DiO and DiD[38, 39], can directly insert into the endothelial lipid layer during transcardiac perfusion, and thereby successfully stain the complete vasculature including the micro-vessels[40]. Nevertheless, considering that most of the clearing methods employ detergents and organic solvents, there is a high risk that along with the lipids also the fluorescent label is removed at some stage of the clearing process. This limitation has been solved by the introduction of DiI analogues such as CM-DiI, SP-DiI, and FM 1–43FX that are modified to be aldehyde-fixable to proteins and CLARITY-compatible[41]. In a recent work, DiI dyes have been incorporated in neutral liposomes for improving vessel painting. These liposomes do not aggregate and thus do not cause vessel clogging[42]. Vascular labelling can also be achieved by means of intracardial or intravenous injection of Evans Blue (EB) that after binding to serum albumin, links the endothelial glycocalyx and is also endocytosed[43]. Lately EB has been administrated together with other molecules such as lectins, to accomplish vascular staining more effectively. In this regard, there are several studies that describe fluorescent lectins as suitable candidates for vascular labelling. Biotinylated tomato lectin is one of such fluorescent lectins that allowed morphological examination of capillaries in different tissues[44]. Although lectins can get rapid access to carbohydrate ligands on the luminal surface of capillary endothelial cells, they are also rapidly cleared from the vessel and therefore when lectins are used for visualization of the vasculature, organs should be harvested quickly after injection[44]. Even if multiple lectins are currently available, the result of a comparative study conducted on Griffonia simplicifolia isolectin B4 (IB4), wheat germ agglutinin (WGA), and Lycopersicon esculentum agglutinin (LEA), suggested that their performance differs depending on specific conditions[45]. Todorov et al. applied a combined approach based on injected EB and perfused fluorescent WGA for mapping the whole vasculature in optically cleared mouse brain[46]. In as much as WGA and EB dyes can be detected in different fluorescence channels this study suggested that the

lectins are indeed more suitable for labelling micro-vessels in brain tissue. In keeping that the inner wall of the vessels is negatively charged, cationic tracers with a proper molecular size can also be used for binding to the negatively charged glycosaminoglycan (GAG) components of the vasculature and basement membranes. Indeed, Huang et al. designed a compound, MHI-148-PEI, in which the branched polyethyleneimine (PEI) is conjugated to a near-infrared (NIR) dye and in combination with ECi clearing, allows to display big vessels and glomeruli in renal tissue[31].

1.4 High resolution imaging of renal tissue

Recent advancements in clearing techniques have allowed the increase of imaging resolution for histological analysis at cellular and subcellular levels. In particular, the use of specific hydrogel for the sample embedding and tissue expansion significantly increased imaging resolution, disclosing structures at nanoscale level. Technological developments in microscopy, i.e. super resolution microscopy (SRM), demonstrated the possibility of achieving spatial resolution beyond the diffraction limit without the need for electron microscopes. For this discovery, dated 2014, Hell and William E. Moerner were awarded the Nobel Prize in Chemistry. Yet, SRM also has some limitations, especially with regard to volumetric imaging. The limitations are due to rapid fluorescence quenching, sensitivity to spherical aberrations, and light scattering[47] and can be partly overcome by making the samples optically transparent and by reducing the RI mismatch. Some tissue clearing methods also lead to sample swelling or expansion (ExM) bringing additional benefits to the image acquisition by SRM. In the field of neuroscience, the combination of SRM and OTC has allowed synapsis study at molecular level in expanded samples of mouse cortex[48]. Similarly, Unnersjö-Jess et al. were able to study the spatial distribution of proteins at the slit diaphragm in intact renal tissue by using SRM on CLARITY-cleared samples that were slightly swelled[49]. In a following study, they also applied ExM on kidney samples for comparing the performance of confocal microscopy (CM) in expanded samples and super resolution stimulated emission depletion (STED) microscopy in non-expanded cleared samples, showing similar results for both approaches[50]. Along with this result, further progress in ExM, have shown that the volumetric expansion factor can be increased up to 10-fold, overcoming the diffraction limit of SRM as well. Recently, a novel ExM protocol has allowed to resolve individual mitochondrial cristae, separated by 70 nm-100 nm distance, by single-step expansion[51]. ExM also enabled the visualization of fine details

of the glomerular filtration barrier including the podocytes foot process, basement membrane, and cytoskeleton[52]. This application is also suitable to identify pathological alterations in foot process morphology at a nanoscale level[50]. Considering that SRM requires access to sophisticated imaging platforms, ExM has proven to be an optimal and cost-effective alternative to obtain high resolution volumetric imaging in kidney research[53]. Meanwhile, new ExM protocols suitable for the analysis of human renal biopsies opened up to future clinical applications. Thus, Expansion pathology (ExPath) combines histopathological assessment and molecular imaging with nanoscale precision of the same sample, by reviving formalin-fixed paraffin embedded material[5].

1.5 Optical imaging and image analysis of cleared tissue

Although light scattering is minimized in optically cleared samples and many advanced methods for fluorescent labelling have been introduced, the availability of appropriate optical instruments are of equal importance for developing an OTC pipeline for addressing specific morphological/functional questions.

Confocal microscopes can be used for the acquisition of thick specimens but due to intrinsic features of the CM, i.e. limited working distance of the objectives, it does not allow image depth larger than a few millimetres. In addition, CM scans the tissue point to point while exposing the sample to continuous laser light scanning that gives rise to photobleaching and phototoxicity[54]. In contrast to CM, light-sheet microscopes are equipped with longer working distance objectives and illuminate sequentially single tissue planes with a thin light sheet, thereby preventing photobleaching. Hence, light-sheet fluorescence microscopy (LSFM) has been employed in multiple studies for imaging whole organs and whole organisms with exceptional imaging speed. The latter only depends on the frame rate of the camera collecting up to hundreds of millions of voxels per second through the use of advanced detectors[55]. As compared to CM, light-sheet microscopes cannot achieve the same spatial resolution due to the limitations in generating sufficiently thin light sheets to cover large fields of view. New advancements in the field of optics, have contributed to circumvent this issue, by introducing laser beam that can illuminate thinner sections[56], as well as by adopting the multi-view approach via simultaneous light-sheet illumination and fluorescence detection along different orthogonal directions that results in improved resolution in all dimensions[57].

Lastly, an important aspect to consider is the compatibility of the clearing methods, especially of the RI matching solution with the instruments for optical imaging and its components. Solvent-resistant dipping objectives, imaging chambers, and the recent

development of objectives with RI ranging from 1.33 to 1.58 represent important steps forward for obtaining an OTC-friendly set-up. Progress in optical systems also warrants the need for powerful computational strategies that address the current boundaries in data storage and analysis of huge datasets deriving from high-resolution imaging of large specimens. Compression and decompression formats can be an efficient solution for data storage. To display big data, BigData Viewer, a framework included in Fiji, helps navigate and visualize large image sequences[58] while for reconstructing 3D volumes the use of BigStitcher makes it possible to stitch unaligned 3D image tiles belonging to terabyte-sized datasets[59]. Following preliminary image processing steps for reconstruction, quantitative image analysis can be tedious and time-demanding if conducted manually. It also very often requires the opinion of expert pathologists and therefore deep learning-based approaches are becoming increasingly popular.

Quantitative analysis of complex images is possible because of automated object segmentation. This is based on algorithms that recognize voxels belonging to similar structure within an image[60]. In this context, the Ilastik toolkit is a machine learning-based framework with an interactive user-friendly interface that allows performing pixel classification through annotations and labels of small subsets of data provided by the user[61]. Once the classifiers are trained, Ilastik workflows can be applied to new data.

More complex segmentation can be performed by applying more advanced machine learning models that can handle bigger datasets and permit an unbiased analysis. Among the deep learning-based approaches, convolutional neuronal network (CNN) with a U-Net architecture became predominant in bioimage analysis as reviewed by Hallou and co-workers[62]. Deep learning analysis was conducted to reconstruct and quantify the 3D vascular network in optically cleared mouse brains[46] and for counting and analysis of glomeruli in renal tissue sections[63].

The current limitation to deep learning models is the extensive amount of data required for training and annotations that cannot be easily generated, especially for ground truth sets. Moreover, despite the efforts of providing pre-trained models and scripts by the scientific community, interventions on the source code and customization are still required. Therefore, in terms of future directions, further work should be focused on making deep learning pipelines more accessible to a large number of researchers who have low coding expertise.

1.6 Aims of the project

The aim of this research project was to implement OTC protocols for the visualization and analysis of biological structures that have key roles in renal pathophysiology. We mainly focused on two OTC methods that have been largely discussed above: ECi-OTC and ExM, with the purpose of reducing the complexity and improving the performance of currently available protocols. Since, ECi clearing was previously optimized by reducing the sample processing time, we defined two pipelines for vascular staining that are compatible with the use of ECi, for improving the quality of the staining and obtaining suitable data for image segmentation.
Essentially, our goals can be summarized as follows:

- Investigating the use of new fluorescent tracers for vascular staining in ECi cleared healthy and pathological renal tissue and other organs.
- Combining an optimized IHC protocol with ECi-OTC, comparing this with a previously established method, and using it to study pathological samples.
- Examining key features of ExM for effective visualization of podocytes in rat and mouse kidney, using optical imaging instruments that are largely available.

2 MATERIALS AND METHODS

2.1 Animals

All animal experiments were conducted in accordance with the German Animal Protection Law and approved by the local authority (Regierungspräsidium Nordbaden, Karlsruhe Germany in agreement with EU guideline 2010/63/EU), under deep anaesthesia. For testing the new fluorescent dyes and implementing all the OTC protocols (ExM and OTC-IHC), 6 weeks-old female C57BL/6 wild-type mice and 6-months-old rats PKD/Mhm (+/+) (autosomal dominant polycystic kidney disease, only homozygous, thus unaffected) were employed. For experiments on pathological samples, the renal tissue was collected from:

- 24-weeks-old pcy/pcy mice (carrying a missense mutation in the nephronophthisis gene Nph3) presenting polycystic kidney disease;
- 16-18 weeks-old mice knock out (KO) for hyaluronan synthase-2 (Has2) presenting vascular abnormalities; the work was carried out in collaboration with Ms Katerina Stripling at Leiden University Medical Center (LUMC) and with the support of Prof. Bernard M. van den Berg, author of a previous publication about the impact of endothelial Hyaluronic Acid (HA) loss on microvasculature[64].

2.2 Sample collection and tissue processing

All the tissue samples were collected after animal perfusion and were subjected to OTC procedures to improve visualization and analysis of renal and vascular structures using three different approaches:

- ECi-based OTC on pre-stained samples during perfusion
- ECi-based OTC and immunostaining (IHC)
- ExM for podocyte visualization.

2.2.1 Animal perfusion

Animals where anesthetized by intra-peritoneal injection of a cocktail of Ketamine (Wirtschaftsgenossenschaft deutscher Tierärzte eG, Germany) and Xylazine (Serumwerk Bernburg, Germany), with a dose of 120 mg/kg BW Ketamine and 16 mg/kg BW Xylazine.

Animal perfusion aims to remove blood from tissues and ensure their preservation by the application of fixating agents. The procedure described here was performed according to a protocol established by Huang et al.[31], where staining of the vasculature can be achieved by including a step before tissue fixation. The retrograde perfusion set-up included a G21 winged infusion set connected to a compressor (Jun-Air compressor, Rio Grande, 117301) and a syringe pump (Chemyx, Fusion 100 infusion pump) by a 3-stage valve. Perfusion of main substances including 0.9% NaCl, pH=7.4 and heparin 5 IU/mL, and 4% Paraformaldehyde (PFA), was conducted with the compressor pump, while staining solutions were perfused at a rate of 1 ml/min via the infusion pump.

The preparation of the animals consisted of an incision on the abdominal skin and a clean cut of the muscle tissue along the *Linea Alba*. Then, the tip of the infusion set was inserted in between the bifurcation of the femoral aorta and fixed by a vascular clamp. Finally, the vena cava was cut immediately before perfusion.

The perfusion protocols consisted of the infusion of saline/heparin solution at 200 mbar for 6 minutes in mice and at 280 mbar for 3 minutes in rats. Optionally, a mid-step for perfusion of a fluorescent cationic dye was also included, where a flush saline/heparin for 1 minute was given to eliminate the excess of the unlinked dye. Afterwards, the animal was perfused with a 4% PFA solution at 200 mbar for 6 minutes (in mice) or at 230 mbar for 3 minutes (in rats) for tissue fixation.

Kidneys and occasionally other organs, (lungs, heart, diaphragm, liver) were collected and incubated under dark conditions for 18 hours in 4% PFA for post-fixation. Subsequently, the tissue was processed for tissue clearing or stored at 4°C in 1x Phosphate buffered saline (PBS) or in 4% PFA for long-term storage.

2.2.2 Sample preparation — ECi-OTC

A fast clearing procedure was also described by Huang et al.[31], based on the use of ethyl-3-phenylprop-2-enoate as a clearing agent (ECi, SigmaAldrich, Germany, STBH5252, R.I. 1.558 at 25°C). This protocol allows to reduce drastically the time required for clearing whole specimens through the use of an automated tissue processor (TP1020, Leica Biosystem, Nußloch, Germany), which works with vacuum and at room temperature (RT). The samples perfused with the fluorescent markers for the vascular staining tested in this project were processed by following the same existing protocol given its reliability and rapidity. Shortly, whole organs were placed

into metal containers, subject to increasing concentrations of ethanol (50%,80%,99%,99%, 45 minutes each), and a step of clearing in ECi for 2 hours. The specimens were then collected and stored in ECi at RT under dark conditions until imaging.

The clearing procedure described above was also adapted for IHC stained samples. To this purpose, thick tissue sections were subjected to IHC after ECi-OTC (post-clearing IHC) as described in Brenna et al.[65] as well as prior to ECi-OTC (pre-clearing IHC) according to an optimized protocol (IHC-ECi)

In order to label the samples before clearing, after perfusion, the mouse kidneys were collected and post-fixed in 4% PFA (overnight only) and 1 mm thick sections were cut by using a Vibratome (VT1200/S, provided by Leica Biosystem, Nußloch, Germany)

2.2.3 Sample preparation — ExM

Mouse and rat kidney samples were perfused, post-fixed overnight in 4% PFA and placed into a 12-well plate filled with gel solution: AHS (Amplifying Hydrogel Solution), and two sodium acrylate (SA)-free gels (Protocol A and Protocol B), for comparing the performance of three different protocols. AHS-gel was adopted for gel embedding of the samples at an early stage of this project to visualize vascular branches and cilia in lungs[66], while the SA-free gels have been adapted from ZOOM (Zoom by hydrOgel cOnversion Microscopy) described in a recent work for expanding brain tissue and other organs[67]. After 2-3 days of incubation in the gel solution, the tissue-gel hybrid was subjected to polymerization by incubating the plate in a humidified chamber at 37°C for 2-3 hours.

Gel composition	Provider; Cat.No	AHS	Protocol A	Protocol B
NaCl	Roth, 0962.1	-	0.65M	1.3M
Sodium Acrylate (SA)	Sigma Aldrich, 408220	10%	-	-
Bisacrylamid	BIO-RAD, #161-0142	0.05%	0.01%	0.005%
40% Acrylamid	BIO-RAD, #1610140	20%	30%	30%
16% PFA	EMS, #15710-S	4%	2%	2%
10xPBS	In-house	1x	1x	1x
VA-0114	FUJIFLM, #277776-21-2	0.1%	0.1%	0.1%

Table 1 The table includes all the chemicals employed to synthetize the gel according the 3 different protocols

After this step, the sample was trimmed to minimize volume, using a sharp razor blade. Next, the gel-tissue-hybrid was processed by cutting 300 µm slices using a vibratome. Thicker specimens instead, cannot easily be imaged and analysed in depth within a short period of time because of the volumetric expansion. Moreover, thinner sections

are easy to handle after tissue expansion and are more rapidly stained. The tissue sections were then placed into a 12-well plate filled with 1xPBS. The optical clearing was performed by lipid removal and protein denaturation in different Sodium dodecyl sulfate (SDS) containing solutions (see Table 2). SA-free gel-embedded mouse kidneys were incubated in a wet chamber in a denaturation solution for 24 hours while rat kidneys for 48 hours, both at 80°C. The AHS-embedded mouse kidneys were incubated for 12 hours at 95°C and for the following 24 hours at 70°C.

Denaturation solution (pH=9)	AHS-embedded samples	SA-free gel embedded samples
SDS (Sigma Aldrich, L4509)	200 mM	200 mM
Boric acid (Merck, 1.00165.0500)	-	50 mM
Tris	50 mM	-
PBS	1x	-
NaCl	200mM	-

Table 2 The table includes all the reagents required to prepare the denaturation buffer in the 3 protocols: AHS, protocol A, and protocol B.

After clearing, the tissue-gel hybrid was washed for 3 hours in 1xPBST (Phosphate buffered saline with 0.5% Tween) under agitation at RT, to eliminate the denaturation solution before the antibody staining.

2.3 Labelling strategies

2.3.1 Fluorescent markers

All the fluorescent molecules for vascular staining that were employed in this project were developed in collaboration with Cyanagen Srl where, Ms. Srishti Vajpayee performed all the experiments concerning the design and the chemical synthesis of the compounds (Bologna, Italy). Therefore, all the spectrophotometric measurements included in this section were provided by Ms. Vajpayee (Figure 2.1-2.4 and table 3).

A list including the dyes tested in this project, is provided in Table 3.

Name	Lot. Number	Absorbance	Emission	Molecular weight
MHI-148-PEI	SV1-014	620 nm	770 nm	Average 70 kDa
SV620C-01-PEI	SV1/013	620 nm	770 nm	Average 70 kDa
MHI-148+PEI	SV1/018	620 nm	770 nm	0.750 + 70 kDa
SV620C-01+PEI	SV1/021	620 nm	770 nm	0.705 + 70 kDa
STAR FLUOR 645™-WGA	SV2/125	648 nm	678 nm	Average 36 kDa
SV680A-02-WS Chitosan	SV3/276	678 nm	720 nm	Average 110 kDa
SV770Z-01-WS Chitosan	SV4/313	770 nm	820 nm	Average 110 kDa

Table 3 Summary of all the fluorescent markers tested for the vascular staining, data provided by Ms. Vajpayee (Cyanagen Srl, Bologna, Italy)

The fluorescent markers were designed by taking into account the characteristics of the biological structures of interest, i.e. renal vessels and capillaries:

- The blood vessel endothelium is constituted by negatively charged GAGs.
- The cut-off of the renal basal membrane is estimated to be around 50 KDa. This value is given by the structure of the glomerular capillaries that is made of fenestrated endothelium (70-90 nm in size), basement membrane (2-8 nm in size), and podocytes (4-11 nm in size).

Therefore, all the characteristics of the molecules employed in our studies can be described as follows:

- They were linked to a positively charged polymer functional for the binding.
- They have a molecular weight>50 KDa to prevent filtration of the molecule into the renal tubules.

MHI-148-PEI and SV620C-01-PEI

In a previous study a cationic molecule, MHI-148-PEI was developed for staining big vessels and glomeruli[31]. For the current research work, its chemical structure was modified to obtain another variant, SV620C-01-PEI. SV620C-01-PEI is a more stable compound, characterized by a higher degree of labelling (DOL) that maintains the same spectrophotometric properties with absorption/emission in the NIR window similar to Cy7-like dyes as illustrated in figure 2.1.

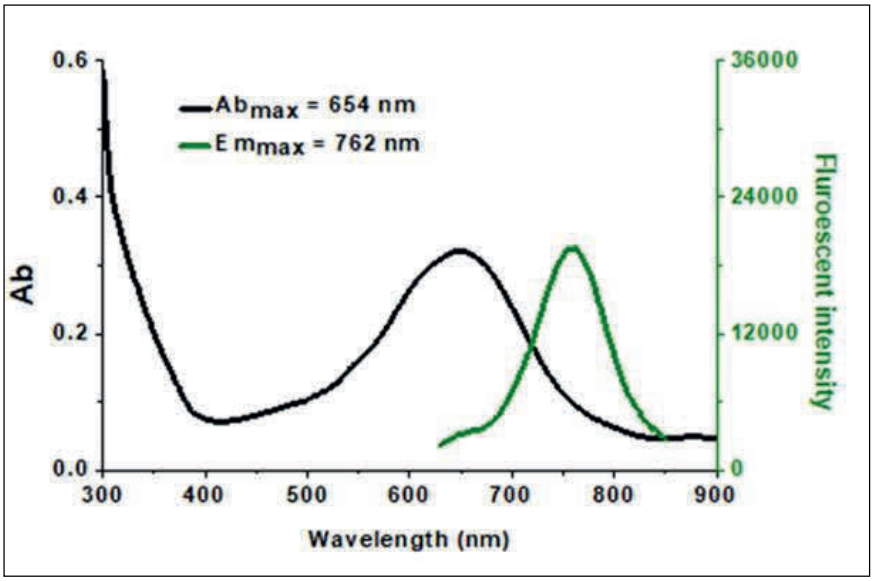

Figure 2.1 Spectrum of MHI-148-PEI and SV620C-01-PEI characterized by a large Stokes shift.

STAR FLUOR 645-WGA

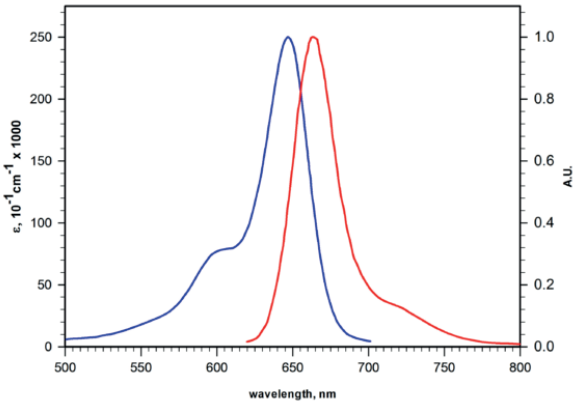

Figure 2.2 Spectrum of STAR FLUOR 645

The WGA is a lectin that can be conjugated to a wide range of fluorophores for labelling biological structures.

The WGA was conjugated to the fluorescent molecule STAR FLUOR 645 that is commercialized by Cyanagen Srl and has an absorption/emission spectrum in the red region of the spectrum as illustrated in figure 2.2.

This fluorophore that has an absorption peak in a similar range to the Cy7-like dyes, ensures higher penetration depth and enables the comparability of the tested compounds. Given its narrow interval of emission wavelengths, it is possible to detect the STAR FLUOR 645-WGA in co-administration with SV620C-01-PEI.

Fluorescent chitosan

Besides the WGA, we tested a polysaccharide that has recently been introduced for biological applications: chitosan. The chitosan molecule is defined by FDA as non-toxic, and is even used as food additive[68].

The polymer was chemically modified by Ms. Vajpayee in order to increase its solubility in water-based buffer as needed for biological studies obtaining water-soluble (WS) - chitosan. The chitosan was covalently conjugated to a NIR and far-red fluorophore and its capability of staining vascular structures was evaluated in comparison with the previous PEI-conjugated molecules.

However, due to the low solubility, anionic and zwitterionic dyes replaced the cationic fluorophores employed previously, without significant impact on the overall positive charge of the molecule, essential for binding the endothelium.

SV680A-02 is an anionic dye that was conjugated to WS-chitosan with an absorption/emission spectrum in the NIR region as illustrated in figure 2.3.

SV770Z-01 is a zwitterionic dye that was conjugated to WS-chitosan with an absorption/emission spectrum in the far-red region as illustrated in figure 2.4.

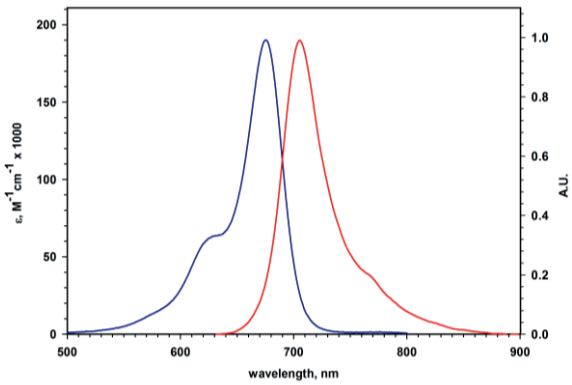

Figure 2.3. Spectrum of SV680A-02 λabs of the dye is at 678 nm and λem is at 720 nm

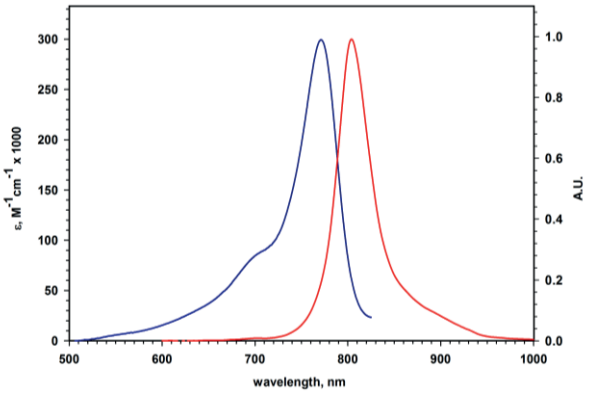

Figure 2.4. Spectrum of SV770Z-01. λabs of the dye is at 770 nm and λem is at 820 nm

2.3.2 Immunostaining and ECi (IHC-ECi)

Samples were incubated for 48 hours in a Dimethyl sulfoxide (DMSO)-based permeabilization solution (1xPBS/0.1%Tween-20/0.1%TritonX-100/ 0.1%Deoxycholate/ 0.1%IGEPAL/ 20%DMSO) at 37°C under shaking.

After 3 washing steps in PTwH (1xPBS/0.2% Tween-20 with 10 µg/ml heparin), they were subjected to a 24 hours-blocking step for reducing the non-specific binding and the background from the samples (6% Donkey Serum, Glyicin 0.3 M, 10% DMSO in PTwH at 37°C).

Thereafter, the double staining was performed in 6 days in 3 steps as described below:

1) Incubation with primary antibody goat anti-CD31 (1:150) in PTwH/5%DMSO/3% Donkey Serum at 37°for 48 h, followed by 3 washing steps in PTwH for 1 hour/each
2) Incubation with primary antibody rabbit anti-podocin (1:50) in PTwH/5%DMSO/3% Donkey Serum, 37°,48 hours, followed by 3 washing steps in PTwH for 1 hour/each
3) Incubation with secondary antibody (anti-rabbit Alexa Fluor 586/Alexa Fluor 594 Plus (1:100) + anti-Goat Alexa Fluor 647 (1:150) in PTwH/3% Donkey Serum) at 37° for 48 hours, followed by 3 washing steps in PTwH for 1 hour/each.

After washing the sample in PBS1x at RT overnight, the samples were subjected to ECi clearing, according to the optimized protocol described above (4 hours, RT).

Reagent	Provider	Cat./Lot. Number
Normal Donkey Serum ab7475	Abcam	GR3234277-28
Glycine	Serva	27052
Tween 20	Fischer scientific	153087
DMSO	Sigma Aldrich	#SZBF3010V
IGEPAL	Sigma Aldrich	#MKBN1103V
Sodium Deoxycolate	Sigma Aldrich	#086K0045V
Heparin Sodium	Serva	24590.02
Anti-CD31: CD31/PECAM-1 (Goat)	R&D Systems	AF3628
Anti-podocin: NPHS2 (Rabbit)	Proteintech	20384-1-AP
Anti-goat Alexa Fluo 647 (Donkey)	Abcam	Ab150131
Anti-rabbit Alexa Fluo 586 (Donkey)	Abcam	Ab175470
Anti-rabbit Alexa Fluo 594 Plus (Donkey)	Invitrogen	# A32754

Table 4 List of reagents and antibodies used for optimizing the immunostaining related to the ICH-ECi protocol

2.3.3 Immunostaining and ExM

The staining of gel-tissue hybrid after sample denaturation was conducted as follows: A short blocking step (blocking buffer: 1xPBS/5%BSA/1%TritonX-100, at 37°C for 24 hr) was followed by incubation in primary antibody (anti-podocin; stock concentration 0.2 mg/ml, diluted 1:100) in 1xPBS/2%BSA/1%TritonX-100 at 37°C for 48 hr. After washing the sample in PBST (37°C, 60 min ×3), was incubated in the secondary antibody (Goat Anti-Rabbit STAR FLUOR 488 conjugated; stock concentration 2 mg/ml, diluted 1:100 or alternatively Donkey Anti-Rabbit Alexa Fluor 647 conjugated diluted 1:100) in 1xPBS/2%BSA/1%TritonX-100 at 37°C for 48 hr. Finally, the sample was washed and stored in 1xPBS, until imaging (rat kidney tissue) or subjected to two rounds of expansion in distilled water for 1 hour (2x) and overnight under shaking (mouse kidney tissue).

Reagent	Provider	Cat. nr.
Bovin Serum Albumin (BSA)	Sigma-Aldrich	#SLCB2779
Triton-X 100	Sigma-Aldrich	#MKBS6557V
Sytox Green™	TermoFisher	S7020

Anti-podocin: NPHS2 antibody [EPR22203-219]	Abcam	ab229037
Anti-rabbit STARFLUO 488 (goat)	Cyanagen srl	F5A166, S001
Anti-Rabbit Alexa Fluo 647 (goat)	Abcam	ab150079

Table 5 List of reagents and antibodies used for optimizing the immunostaining related to the ExM protocol

2.4 Microscopy

Microscopic examination of the cleared specimens was mainly conducted by the Leica TCS SP8 confocal microscope and the Leica TCS SP8 DLS light-sheet microscope. The complete list of instruments is illustrated in table 6.

This set-up was suitable for the acquisition of expanded samples and whole tissue sections because of the better XY resolution accomplished by CM and the possibility to mount wide samples, respectively.

LSFM was preferred for imaging samples in depth instead. The DLS TCS SP8 is provided with a detection objective that includes a mirror cap, where the mirrors are orientated at 45° and, due to that, the specimen should fit in the space created by this orientation and the height of the sample should not exceed 1 mm in order not to touch the lens of the objective. These technical requirements limit the imaging of bigger sized samples along the X and Y axis, however, given the significant reduction of acquisition time and the improved Z-resolution, this technology was strictly chosen for acquiring large Z-stack. The additional imaging systems employed in this project were made available at Leica Microsystem (Mannheim, Germany). Stellaris 8 features a next generation white light laser capable of excitation in any wavelength between 440 nm and 790 nm paired with matched hybrid detectors, that made possible to test far-red fluorescent molecules.

The early evaluation model of light-sheet allows free stage navigation in X and Y overcoming the limitations of the DLS TCS SP8.

Equipment	Manufacturer
Light-sheet microscope – DLS TCS SP8	Leica Microsystems, Germany
Confocal microscope – TCS SP8	Leica Microsystems, Germany
Confocal microscope – Stellaris 8	Leica Microsystems, Germany
Light-sheet microscope early evaluation model	Leica Microsystems, Germany

Table 6 List of all the set-ups for performing ex-vivo 3D imaging employed in this project

2.5 Image acquisition

Data were acquired by LAS X software (Leica Microsystem, Germany) and were stored in the Scientific Data Storage (SDS), of the Computing Center of the University of Heidelberg (Germany).

CM-imaged samples were acquired as follows:

- ECi cleared samples:

  The acquisition speed of 600Hz and the scan direction set to Bidirectional were kept constant while the format (resolution) varied between 1024*1024 pixels (single tile scan) or 512*512 pixels (multi-tile scan) in order to balance the acquisition time and the quality of the pictures for the imaging of large specimens. The tissue sections were imaged by 16x objective, 20x objective, and 40x objective and were mounted by using immersion oil (Merck, Cat. No.1046990100, RI 1.51)

  The samples were glued on the centre of the dish. A solvent-resistant dish was used for imaging ECi-cleared specimens, that was then filled with immersion oil, and a long-working distance objective (16x) was employed to maximize the imaging depth.

  Alternatively, the samples were mounted using a spacer (Grace Bio-Labs CoverWell™ imaging chambers 0.6 mm), by placing it on a glass slide for creating a proper-sized imaging chamber by adding a cover glass on the top. This method was selected for acquiring Has2 longitudinal sections by shorter working distance objectives (20x and 40x) for flattening the sample surface and reducing overexposure issues moving along X and Y axis when modulating the exciting laser power through the sample depth (Z-compensation).

- ExM processed samples:

  The acquisition speed was reduced from 600Hz to 400Hz (not bidirectional), the format (resolution) was set to 2048*2048 pixels and the pinhole was reduced from 1.0 to 0.6 Airy Unit (AU) for improving lateral resolution. For ExM factor calculation, the speed was kept at 600Hz and the format at lower resolution (1024*1024 pixels). The samples were imaged by a 63x objective with high Numerical Aperture (NA) for an increased axial resolution and were mounted by agarose embedding.

  The tissue-gel hybrid was placed at the centre of a glass and melted 2% agarose (Invitrogen UltraPure Low Melting Point Agarose, Thermosfisher Scientific, Germany, 16520100) was added surrounding the sample by producing 1 or 2 layers in order to immobilize the sample and to prevent movements during the imaging.

The dish was then filled with 1xPBS (rat kidney tissue) or with the distilled water used for expansion (mouse kidney tissue).

LSFM imaged samples were acquired as follows:

The acquisition speed was set to 600 Hz and the usual resolution was set to 2*2 binning. The specimens were imaged by ECi-resistant objectives (5x and 16x objectives) and were mounted by using ECi as an immersion medium.

The sample was anchored by sticking a piece of parafilm of 1 mm in thickness (to avoid the direct contact of the objective's mirrors with the bottom of the dish) in the centre of a glass bottom cell culture dish (35 mm high, 60 µm in diameter, IBIDI, Martinsried, Munich, Germany). On that, a piece of the specimen, a maximum of 0.4 mm in width and 0.5 mm in height was pasted by using the superglue. Finally, the dish was completely filled with ECi.

The detailed description of the objectives is illustrated in the table below (Table 7).

Microscope	Objective	Working distance	Mounting media
Confocal	HC APO L-U-V-I 63x/0.90 (Leica Microsystems, Germany)	2.2 mm	Distilled water (R.I. 1.33 at 25°C)
Confocal	40x/1.25 OIL (Leica Microsystems, Germany)	0.1 mm	Immersion oil (R.I 1.51 at 23°C)
Confocal	HC PL APO CS2 20x/0.70 IMM (Leica Microsystems, Germany)	0.6 mm	Immersion oil (R.I 1.51 at 23°C)
Confocal	HC FLUOTAR 16x/0.60 IMM (Leica Microsystems, Germany)	1.6 mm	Immersion oil (R.I 1.51 at 23°C)
Light-sheet	HC PL FLUOTAR 5x/0.15 IMM DLS (Leica Microsystems, Germany)	1.5 mm	ECi (R.I. 1.558 at 25°C)
Light-sheet	HC FLUOTAR L 16x/0,60 IMM CORR DLS (Leica Microsystems, Germany)	2.5 mm	ECi (R.I. 1.558 at 25°C)

Table 7 Description of the different objective employed throughout the project and of their features

2.6 Quantitative image analysis

2.6.1 Glomerular analysis in Has2 mice

Image acquisition was performed using Leica Application Suite X (LAS X v.3.5.6, Leica microsystems) by randomly selecting 15 regions of interest (ROIs) in the cortical area of each longitudinal renal tissue section. The optical subset was cropped by using the selection tool in ImageJ in order to obtain sub-volumes of 0.9 mm^3.

Image processing was performed using Fiji (ImageJ 1.52p).

The sub-volumes were split into the 3 acquisition channels and the autofluorescence channel was subtracted from the podocin channel for background removal. Thereafter, the podocin channel was analysed as follows: [background subtraction=20, value set after observation of the pixel values in the selected areas through line profiler function in ImageJ] > [Gaussian blur filter σ=3]. After pre-processing the CD31 channel [3x3x3 Median filter], the two channels were overlaid, converted to RGB, and exported as .HDF5 format. Subsequently, images were segmented using pixel classification in Ilastik (v1.3.2) with a trained classification for background and glomeruli. The resulting segmented data were exported as simple segmentation .HDF5 files. Glomerular parameters were assessed by doing a connected component analysis using ImageJ: 3D Objects Counter and 3D ImageJ Suite (3DSuite) on segmented files[69].

2.6.2 Expansion factor calculation in rat and mouse renal tissue

For calculating the expansion factor in expanded rat and mouse tissue, we compared the maximal nuclear diameter three-dimensionally by taking into account 3 different areas (ROIs) per representative sample of non-expanded gel-tissue hybrid and of the corresponding expanded tissue, both stained with Sytox green. In this way, for each ROI the mean values of Feret diameter were measured in tissue before expansion and in tissue after expansion. The ratio of the mean diameter of post-expansion nuclei and of pre-expansion nuclei can be considered an estimation of the linear expansion factor and was evaluated in protocol A and protocol B. The images were acquired by using Leica Application Suite X (LAS X v.3.5.6, Leica microsystems), and then, 3 large subsets were selected in the cortical area of renal tissue sections and cropped by using the selection tool in ImageJ. The .tif files were segmented by using Cellpose[70] to obtain a binary mask and the segmented data were selected through a shape filter [roundness filter=0.7]. The diameter was estimated using ImageJ plug-in MorpholibJ by running a Groovy script.

2.6.3 Signal-to-noise ratio measurement in IHC-cleared kidneys

SNR was calculated by acquiring small volumes of two IHC-ECi sections from the same animal that were processed differently (with and without additional fixation step in PFA). The podocin channel was selected and 10 subsets were cropped to determine mean intensity values (μ) and standard deviation (σ) of background and glomerular signal. The optical subset was cropped by using the selection tool in ImageJ in order

to analyse sub-volumes containing a single glomerulus. Briefly, a median filter [3x3x3] was applied to the images and a threshold range was manually set in upper regions of the sample, to cover areas defined as glomerulus, and converted into binary masks; by inverting the mask, the binary mask of the background was obtained as well. ROIs generated from binary masks were used to automatically measure mean background intensity in the original stacks. The SNR was calculated for each stack according to the following equation[71]:

$SNR = \mu_{SIGNAL} / \sigma_{BACKGROUND}$

2.6.4 Statistical analysis

Continuous variables were expressed as means ± standard deviation (SD). The variables were normally distributed and were analysed with student's t-test for two independent groups. All analyses were performed with JMP (v.15.0.0).

3 RESULTS

3.1 ECi and perfused fluorescent dyes

3.1.1 Comparison of MHI-148-PEI and SV620C-01-PEI

Although it has been shown that MHI-148-PEI is a good marker for the visualization of large vessels and glomeruli in kidney tissue, several drawbacks were previously identified. In particular, batch-to-batch variation of MHI-148-PEI in terms of degree of labelling (DOL) of the polymeric component and its low stability over time, are the main hurdles that hamper standardization of MHI-148-PEI and its use in OTC. To address these shortcomings, we first compared different mixtures of the dye and the polymer with an optimized variant, SV620C-01, to elucidate the underlying mechanism responsible for variation and stability. To this end, MHI-148-PEI was either tested as a covalent conjugate or as a mixture of uncoupled MHI-148 and PEI. SV620C-01-PEI conjugate and mixtures of SV620C-01 and PEI were tested similarly.

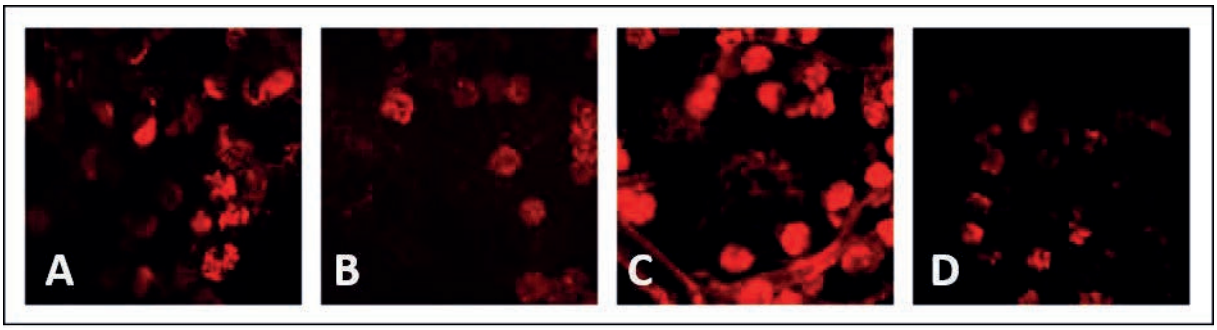

Figure 3.1. Sections of a mouse kidney (in maximum projection), acquired by CM using a 16x objective in immersion oil, 638 channel. Staining: A) MHI-I48-PEI; B) MHI-I48+PEI; C) SV620C-01-PEI; D) SV620C-01+PEI. The compounds were tested at the same concentration (3 mg/mL) and experimental conditions.

As demonstrated in figure 3.1, the MHI-I48-PEI conjugate (A) and MHI-148+PEI mixture (B) gave comparable results showing a similar labelling capability of glomerular structures. For the conjugated SV620C-01-PEI (C), both glomeruli and vessels are stained and signal detection was possible at low laser power, while the unconjugated mixture (D), only mildly and partly stains glomeruli.

Spectrophotometry revealed that both the absorption and emission peaks of SV620C-01 are higher than the values measured for the MHI-148 when conjugated to the PEI, due to the known lower DOL of the polymer that characterize the MHI-I48-PEI conjugate (Figure 3.2). Given its higher fluorescence intensity and its superior photo-stability over time (data not shown), SV620C-01-PEI was used throughout the project for implementation in existing protocols and for studying preclinical models.

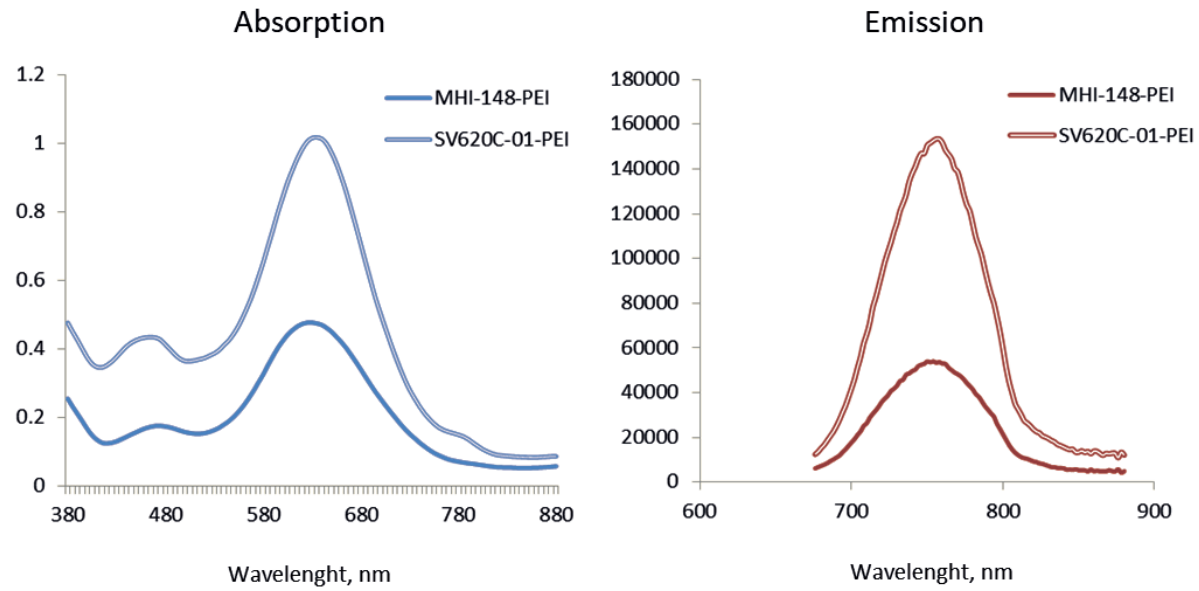

Figure 3.2 Absorption (left) and emission (right) spectra of MHI-148-PEI and SV620C-01-PEI in comparison.

In the following paragraphs, specific aspects of the performance of the SV620C-01-PEI conjugate (e.g. different set-ups for imaging, dose-dependency, pathological samples, suitability of the data for 3D image analysis) are addressed.

3.1.2 SV620C-01-PEI: dose-dependency

Dose dependency was assessed by addressing to what extent variations in SV620C-01-PEI concentration of the perfusion solution influences the labelling performance.

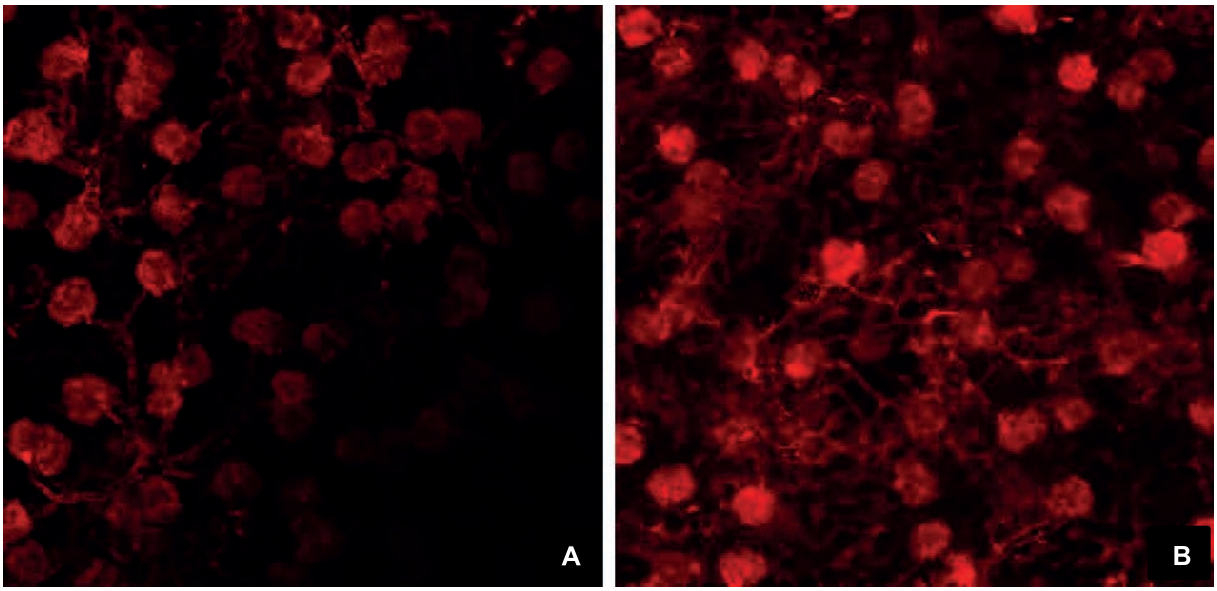

Figure 3.3. Sections of mouse kidney (maximum projection), acquired by CM using a 16x objective in immersion oil, 638 channel. Staining: A) SV620C-01-PEI, 0.5 mg/mL; B) SV620C-01-PEI, 2 mg/mL.

The dose of SV620C-01 for perfusion that was initially tested was equivalent to 3 mg/mL as originally employed for MHI-148-PEI. Based on the higher DOL of the PEI

and higher absorption/emission peak in the infrared range, the concentration of SV620C-01-PEI was decreased to 1 mg/mL. These spectrophotometric measurements provide, exclusively information about the fluorescent – but not about the polymeric component that carries more positive charges for binding to negatively charged biological structures. For this reason, we compared two additional doses, 2 mg/mL and 0.5 mg/mL. Although at 0.5 mg/mL, glomeruli and vasa afferent are visible in cortical sections of mouse kidneys (Figure 3.3 A), a higher laser intensity power was required for visualization as compared to the higher dose of SV620C-01 (2 mg/mL) (Figure 3.3 B).

Even though the higher concentration of the marker might better visualize smaller capillaries at lower excitation power (laser power: 1.2% for 0.5 mg/mL versus 0.6 % for 2 mg/mL), the inhomogeneous distribution of the marker in vascular structures may give rise to overexposure issues. Therefore, a working concentration of 1 mg/mL was chosen for all further experiments.

Figures 3.4 and figure 3.5 show a large volume of renal tissue harvested from mice perfused with the above-mentioned dose of SV620C-01-PEI that were acquired at high depth respectively by CM and LSFM.

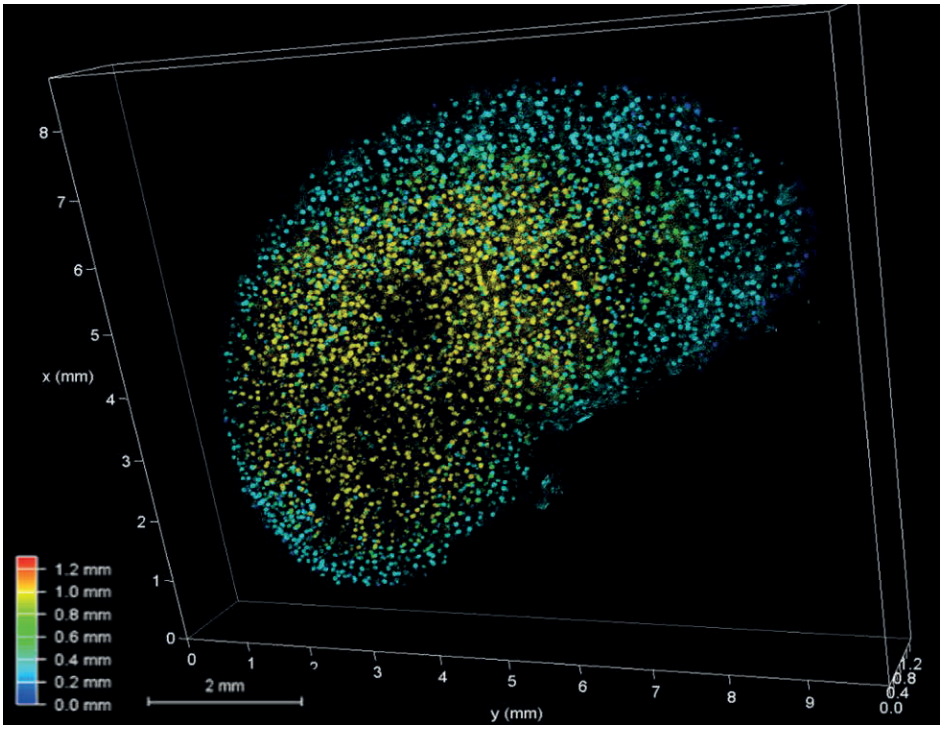

Figure 3.4 Intact mouse kidney (3D) imaged by CM using 16x immersion oil objective, 638 channel. Staining: SV620C-01-PEI (1 mg/mL). Color-coded image to improve depth perception from yellow (closer) to blue (further). Scale bar: 2 mm

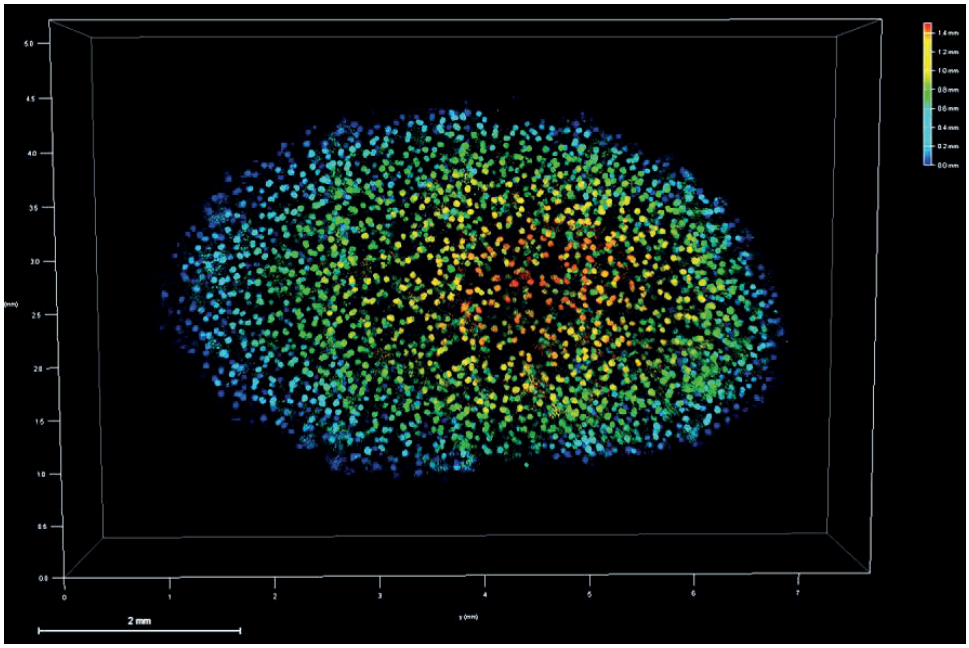

Figure 3.5 Intact mouse kidney (3D) imaged by LSFM using 5x objective in ECi, 638 channel. Staining: SV620C-01-PEI (1 mg/mL). Color-coded image to improve depth perception from yellow (closer) to blue (further). Scale bar: 2 mm

3.1.3 SV620C-01-PEI: applications in preclinical models

We next investigated if SV620C-01-PEI can be used for visualization of vascular structures in pathological samples. The autofluorescence signal, detected in the 488-552 nm range, is enhanced after the ECi clearing and provides supplementary morphological information. As can be seen in figure 3.6. SV620C-01-PEI can be employed for imaging morphological changes as well as for the qualitative assessment of the vascular damage in Nephronophthisis (NPH) disease.

A

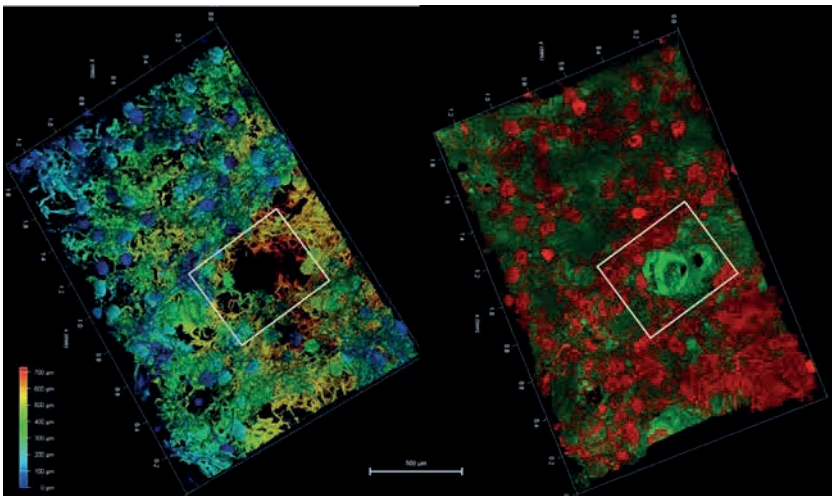

B

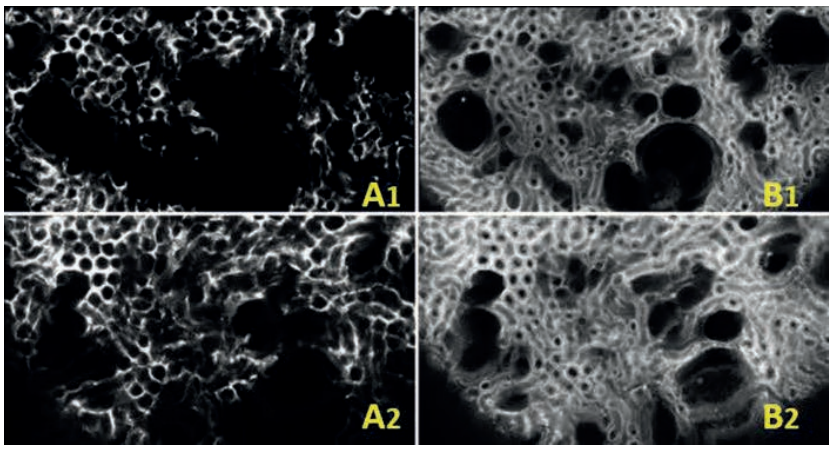

Figure 3.6 CM imaging of a pcy mouse kidney section performed using 16x objective in immersion oil. Pcy mice were perfused with SV620C-01-PEI (red, 638 nm) and hereafter cleared by ECi.
3.6 A: On the left a 3D representation of the vasculature is shown using a color-coded depth (yellow: close; blue: far). On the right an overlay with the autofluorescence background (green, 488 nm) is shown. The white frame represents a typical pathological lesion. Scale bar: 500 µm
3.6 B: 2D-representation of the lesion captured at two different depths. A1 and A2 depict the SV620C-01-PEI staining revealing a discontinuous vasculature, B1 and B2 depict the autofluorescence, revealing loss of tubular formation.

3.1.4 STAR FLUOR 645-WGA and SV620C-01-PEI

In order to improve labelling of the renal vasculature by SV620C-01-PEI, a perfusion protocol was implemented with the use of fluorophore-conjugated WGA. To this end, the staining performance of the WGA-STAR FLUOR 645 conjugate in mouse kidney tissue was first evaluated independently and subsequently in combination with SV620C-01-PEI. The rational for the combination was to elucidate if the WGA conjugate could improve the staining-performance of the SV620C-01-PEI given the limited efficiency to label smaller vessels of the latter conjugate. Perfusion of all compounds was performed sequentially at 1 ml/min rate. The compounds were used at iso-absorbic concentrations, i.e. equivalent absorption peak of the two compounds, which translates into an equal amount of dye and not of polymer.
We observed that although STAR FLUOR 645-WGA stains capillaries in the cortical area of the mouse kidney (Figure 3.7), it is not possible to track the vascular network completely especially not at the peritubular level without overexposing the sample.

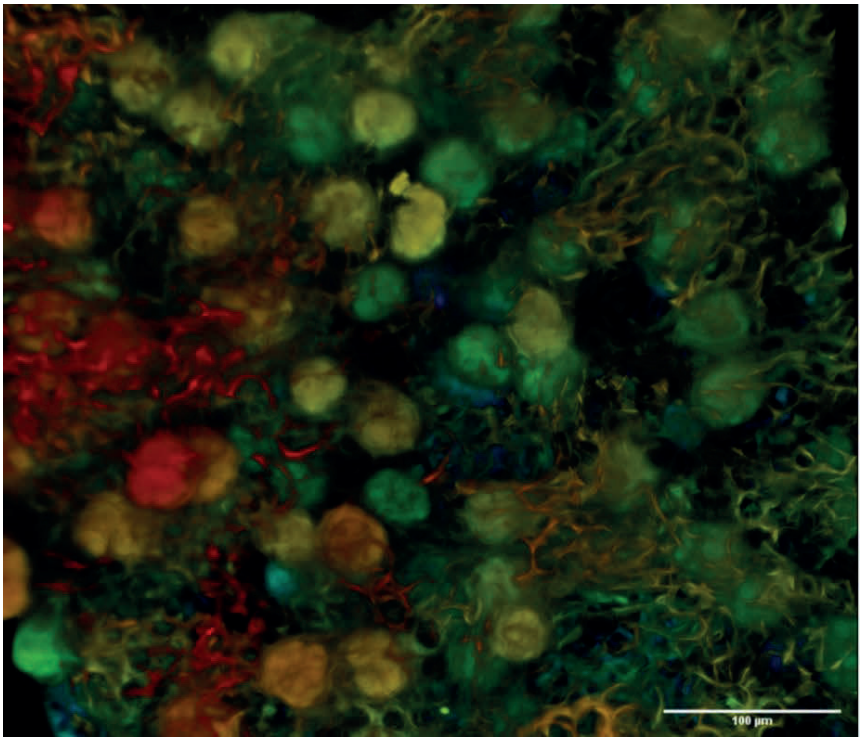

Figure 3.7 Mouse kidney pole (maximum projection) imaged by LSFM using 16x objective in ECi, 638 channel. Staining: STAR FLUOR 645-WGA. Color-coded image to improve depth perception from red (close) to blue (far). Scale bar: 100 µm

As compared to STAR FLUOR 645 conjugate alone, the combination of FLUOR 645-WGA and SV620C-01-PEI revealed a more pronounced labelling provided by the WGA- (yellow) as compared to the PEI-conjugate (red) (Figure 3.8). Due to the higher emission peak of STAR FLUOR 645, this was likely caused by the superior brightness of the fluorophore rather than by a higher labelling efficiency of the vessels.

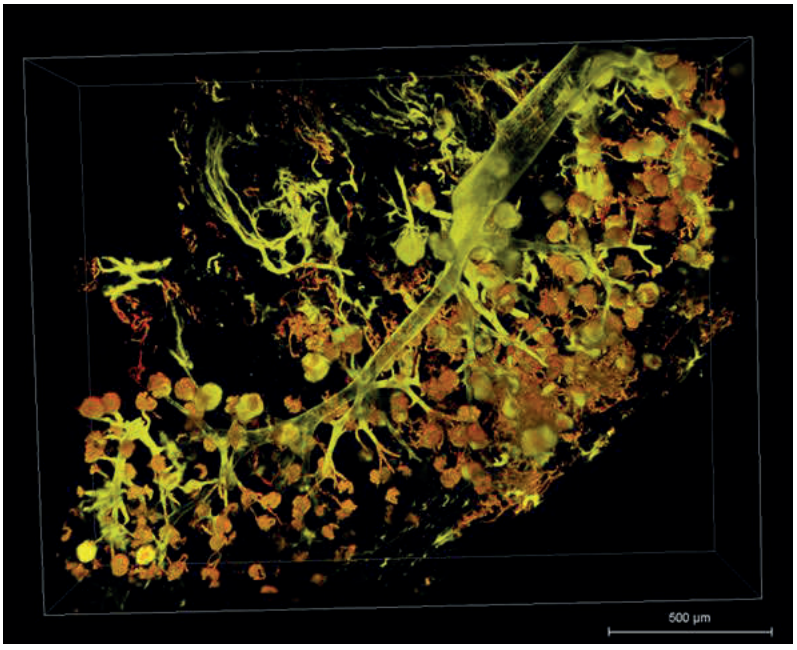

Figure 3.8 Mouse kidney (3D) imaged by CM using a 16x objective in immersion oil, 638 channel. Staining: STAR FLUOR645-WGA (yellow) and SV620C-01-PEI (red) in overlay. Scale bar: 500 µm

3.1.5 Fluorescent chitosan in renal tissue

In order to address the limited labelling performance of the molecules tested in the study presented above, a novel fluorescent cationic polymer was taken into consideration. Chitosan replaced PEI and was conjugated to fluorophores with improved optical properties. In fact, none of the new molecules showed an additional absorbance peak in the 488 nm channel, which is used for the acquisition of endogenous autofluorescence for providing background morphological information.
The use of chitosan for biological experiments requires chemical modifications that improve water solubility at physiological pH. The WS chitosan was conjugated to a far-red and to a NIR fluorophore. Both the far-red SV770Z-01 and the NIR SV680A-02 dyes allowed visualization of the vascular structures in the kidney in depth, including the finest structures such as the peritubular capillaries (Figure 3.9, respectively A and B). A direct comparison of the vessel staining performance for the SV620C-01-PEI (A) and two chitosan conjugates (B and C) is shown in figure 3.10. The NIR Chitosan conjugate also stained the vasculature in other tissues such as muscle and liver (Figure 3.11).

A

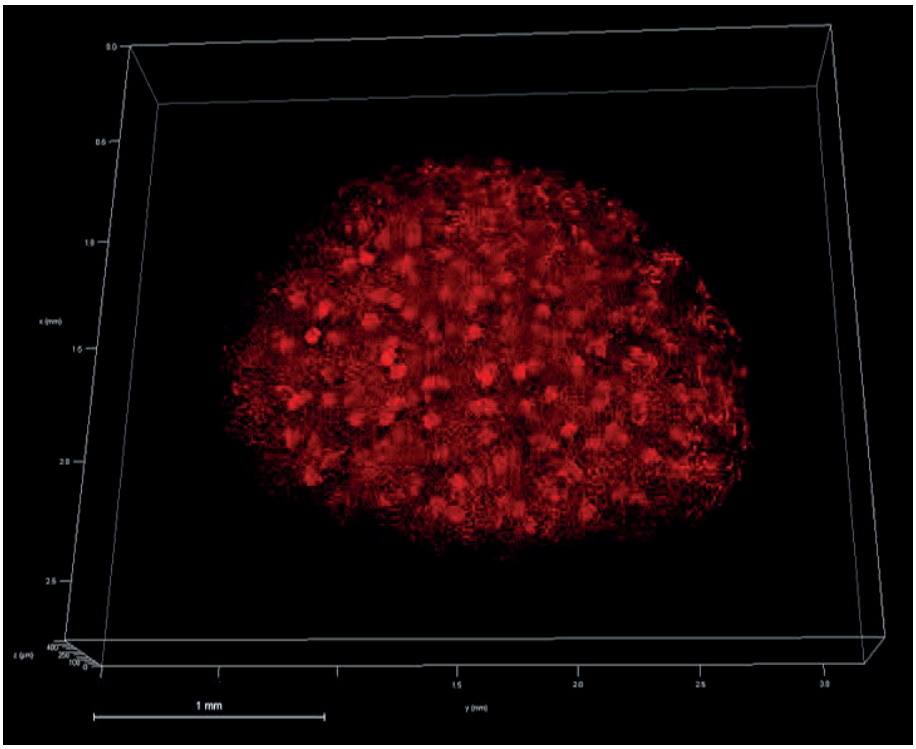

B

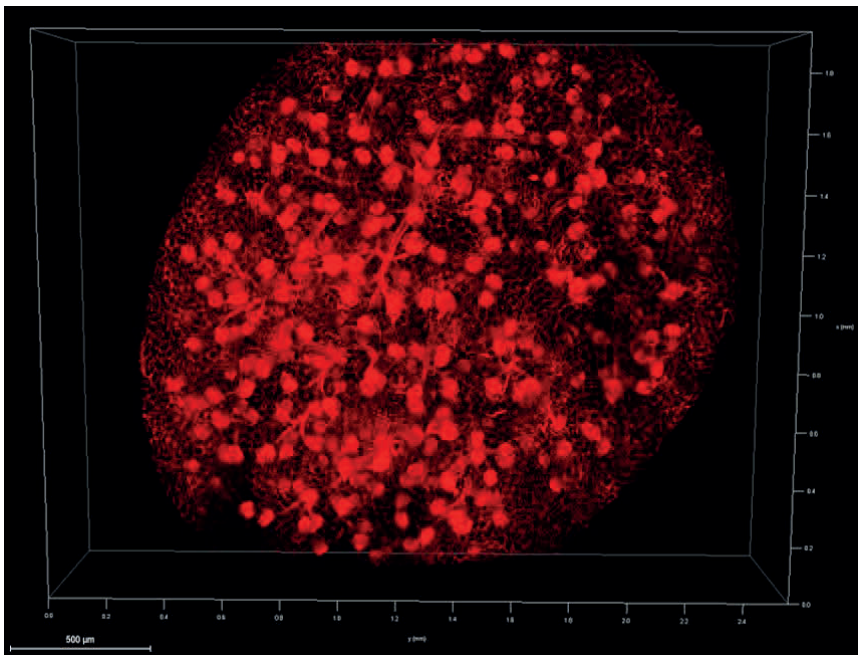

Figure 3.9 ECi cleared mouse kidney pole stained with fluorescent chitosan and imaged by CM using a 16x objective. A: Staining: SV770Z-01-WS Chitosan detected at 770 nm (Stellaris 8); scale bar: 1mm. B: Staining: SV680A-02-WS Chitosan detected at 638 nm; scale bar: 500 µm

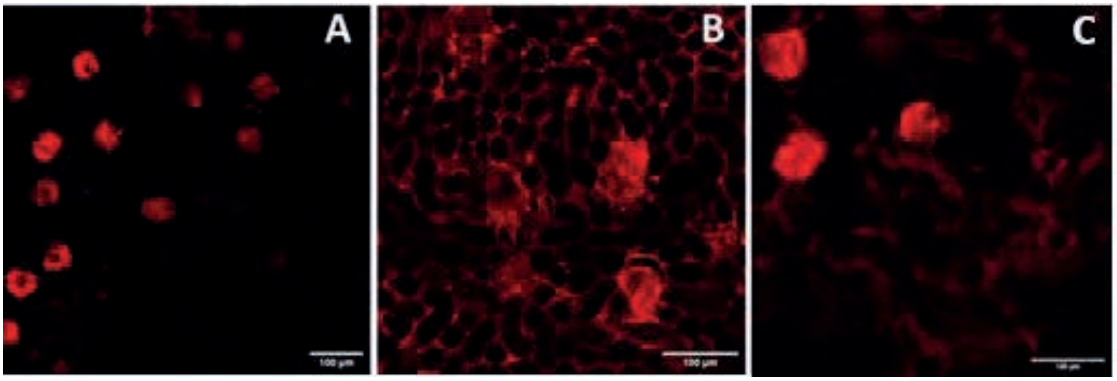

Figure 3.10 Sections of a mouse kidney (2D), acquired by CM using a 16x objective in immersion oil/ECi. Staining: A) SV620C-01-PEI; B) SV770Z-01-WS Chitosan; C) SV680A-02-WS Chitosan. Scale bar: 100 µm

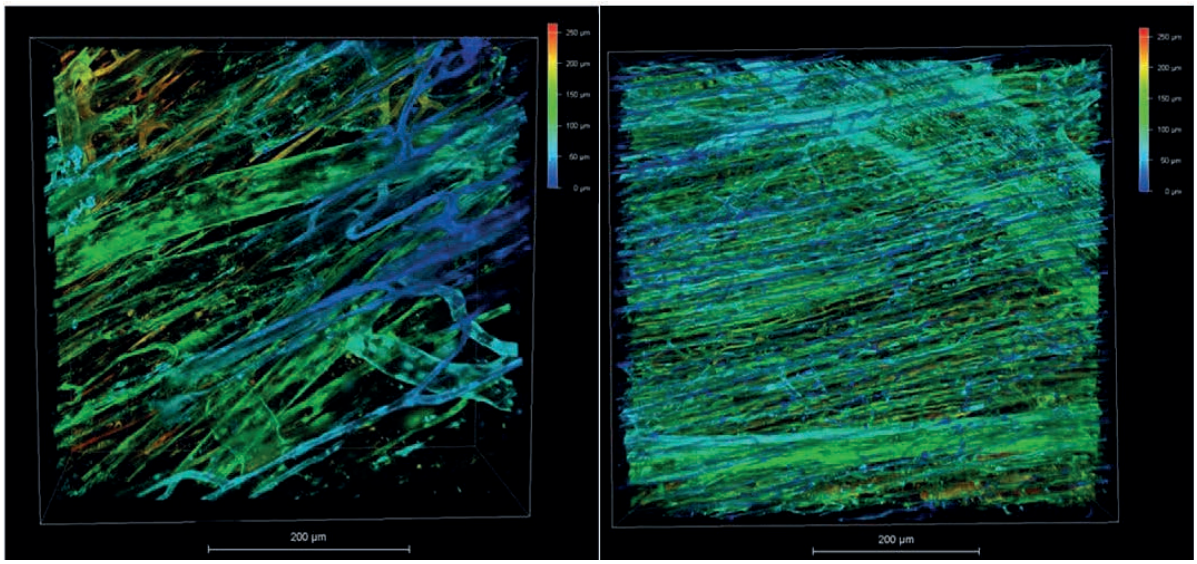

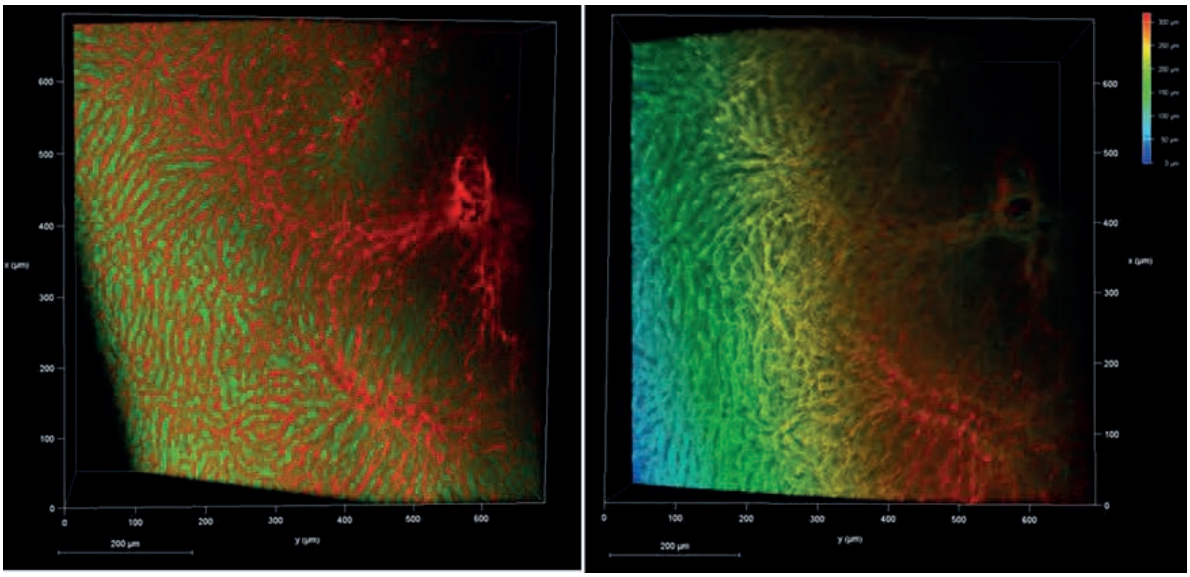

Figure 3.11 Perfusion with SV680A-02-WS-chitosan allows the detection of the vasculature in other tissues. Upper panels: sections of mouse diaphragm, lower panels: sections of mouse liver. Images were acquired by CM using a 16x objective in immersion oil. SV680A-02-WS Chitosan (red, 638 nm), autofluorescence (green, 488 nm). Color-coded images are shown to improve depth perception from red (close) to blue (far). Scale bar: 200 µm.

3.2 IHC and ECi

The use of specific antibodies allows the labelling of specific target structures of interest. The disadvantage of immunolabeling, however, is that it requires long incubation times as compared to the administration of fluorescent tracers. We sought to establish a 3D-IHC protocol combined with ECi clearing for the analysis of the renal vascular structure in thick tissue sections.

3.2.1 Protocol optimization

We first performed immunofluorescence after ECi clearing by rehydrating the samples after the clearing (post-clearing IHC) according to the 3D-IHC protocol described by Brenna et al.[65]. The pitfalls of this method are the long turn-around time, the use of a large amount of primary antibodies and their poor penetration depth. The optimization included performing antibody staining before ECi clearing (pre-clearing IHC) according to an optimized protocol (IHC-ECi) that reduces the total sample processing time as shown in figure 3.12 (in orange)

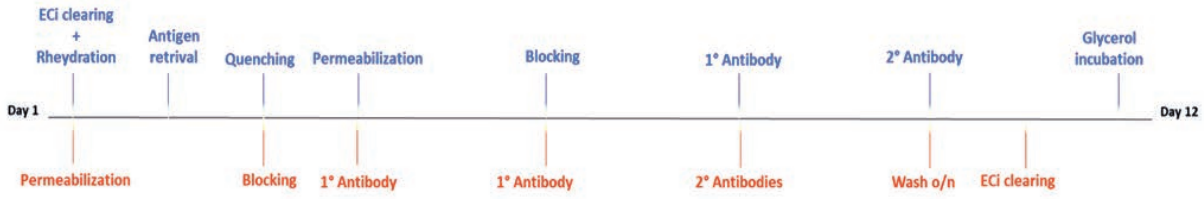

Figure 3.12 Timeline for samples processing according to the protocol before the optimization (in blue) and after the optimization (in orange). The diagram underlines that it is possible to achieve dual antibody staining in shorter time after optimization (dual antibody staining in 10 days vs. single antibody staining in 11 days)

We combined the antibody staining described in Ranier et al. with our ECi-based protocol, by condensing some steps of the original immunolabeling enabled-3D imaging of solvent-cleared organs (iDISCO) procedure and without including the methanol-based-pre-treatment of the tissue[72]. This resulted in a significantly shorter turn-around time, improved tissue clearing performance, and consequently improved optical imaging by CM. Moreover, with these modifications, we achieved good results in terms of antibody penetration and specificity. In table 8 a detailed schematic description of changes for protocol optimisation is presented. Two mouse kidney sections were processed according to the two different pipelines and data acquisition was done by CM using the autofluorescence signal at 488 nm and the Alexa Fluor 647 signal at 638 nm to detect podocin. Although both pipelines allowed the detection of podocin, the optimized protocol, IHC-ECi, enabled visualization of renal structures in depth up to 250 µm, while limited to 100 µM by the former protocol (Figure 3.13).

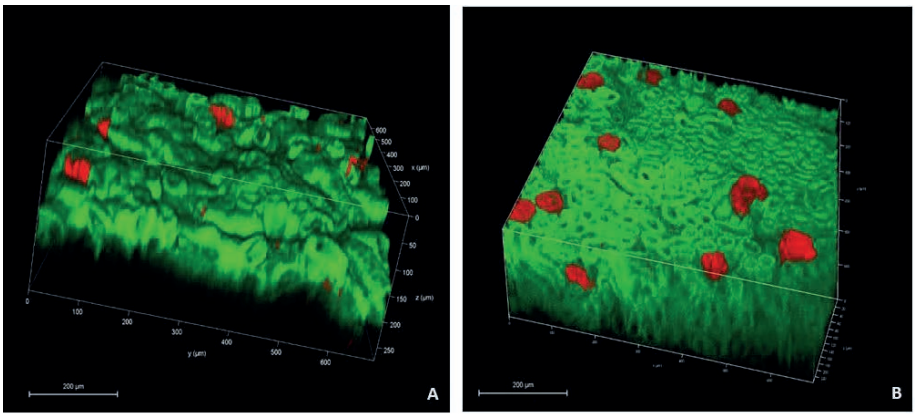

Figure 3.13 Sections of a mouse kidney (3D) acquired by CM using a 16x objective in immersion oil. Staining: Alexa Fluor 647 to detect Podocin in 638 channel (red) and autofluorescence detection in 488 channel (green). A) former protocol (post-clearing IHC); B) optimized protocol (pre-clearing IHC). In both the samples, Z-compensation was applied for imaging in order to improve the maximum acquisition depth. Scale bar: 200 µm

Optimized IHC-ECi protocol			
Steps	Reagent	Time	Total Time (days)
Permeabilization	DMSO-based permeabilization solution	48 hours	
Blocking	Specific serum-based buffer	24 hours	10 days
Antibody staining	Double staining (CD31 and podocin)	48 hours (3x)	
Dehydration	Ethanol (50%-80%-99%-99%)	4 hours	
Clearing	ECi (RI= 1.56)	Overnight	
Protocol described previously[65]			
Steps	Reagent	Time	Total Time (days)
Dehydration	Ethanol (50%-80%-99%-99%)	4 hours	
Clearing	ECi	overnight	11 days
Rehydration	Ethanol (99%-99%-80%-50%) – PBS1x	4 hours-overnight	
Antigen retrieval	Citrate buffer pH 6.0	Overnight	
Quenching	500 mM Glycine	24 hours	
Permeabilization	TritonX100-based solution	48 hours	
Blocking	Specific serum-based buffer	48 hours	
Antibody staining	Single antibody staining (CD31 or podocin)	48 hours (2x)	
RI matching	Glycerol 88% (RI=1.45)	24 hours-weeks	

Table 8 Sample processing workflow for IHC and ECi. Comparison between optimized protocol and former protocol

We next tested CD31 staining in mouse kidney sections to track the renal vessels and capillaries. As can be seen in figure 3.14, the renal vasculature of the mouse kidney was completely stained and allowed tracking from cortical areas towards the outer medulla by CM.

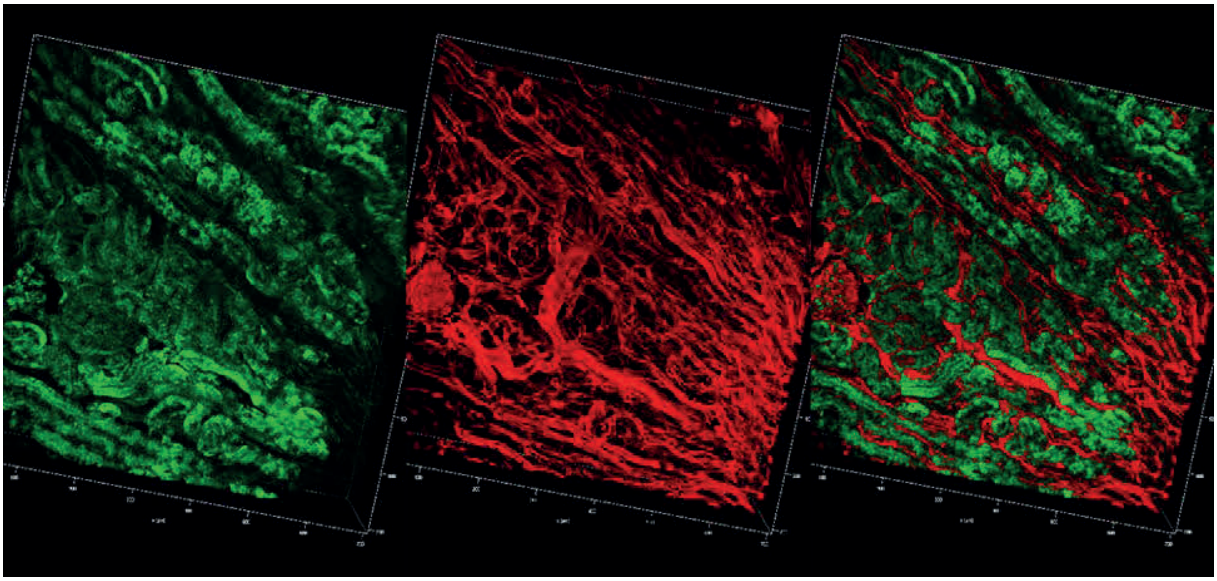

Figure 3.14 Sections of mouse kidney (3D) acquired by CM using a 16x objective in immersion oil. Staining: CD31 was detected by Alexa Fluor 647 in the 638 channel (red) and autofluorescence detection in the 488 channel (green). Scale bar: 200 µm

Similar to described for CM, the CD31 stained sections were also analysed by LSFM for comparing the maximal acquisition depth in samples subjected to post-clearing IHC or to pre-clearing IHC protocol. This was carried out to evaluate how light scattering affects imaging along the whole thickness of the sample without applying Z-compensation. The latter is required for CM and could create some imaging artefacts, e.g. overexposure, and background.

The results (Figure 3.15) obtained from samples processed according to the optimized protocol, show that it is possible to acquire images with sufficient sharpness up to 600 µm by LSFM. Instead, the acquisition depth in rehydrated samples processed according to the former protocol is below 100 µm and in line with the previous conclusions made for the CM-imaged samples (Figure 3.13).

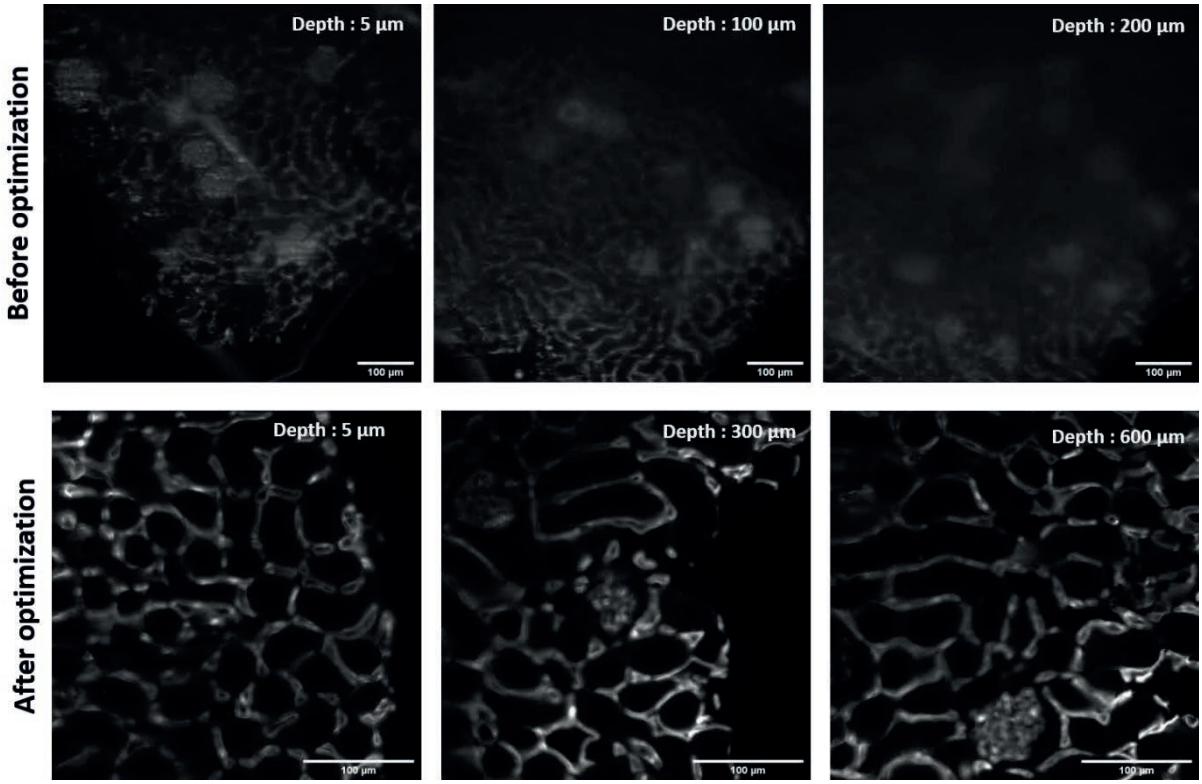

Figure 3.15 Sections of mouse kidney acquired by LSFM using a 16x objective in ECi. Samples processed according to post-clearing IHC (before optimization, upper panel) and to pre-clearing IHC protocol (after optimization, lower panel) at different magnification (refer to scale bars). Staining: CD31 detected by Alexa Fluor 647 in 638 channel (grey scale). From left to right different Z-plan at progressive depth are represented. Scale bar: 100 µm

3.2.2 IHC-ECi Dual Staining

The optimized protocol was implemented for double immunolabeling of thick tissue using anti-CD31 and anti-podocin to visualize vessels and podocytes in the glomeruli of mouse kidneys. Image acquisition was performed in 3 channels, i.e. 488, 552 and 638 nm. The presence of a strong background is very common in thick specimen especially after ECi clearing of fixed tissue. Hence, the use of PFA for tissue fixation was also examined. Combining tissue clearing with immunolabeling very often involves further post-fixation of the tissue, which enhances background autofluorescence. Post-fixation was not required when ECi clearing was used. In figure 3.16, two samples imaged by CM are compared showing that over-fixation in PFA (on the left) reduces the signal-to background ratio.

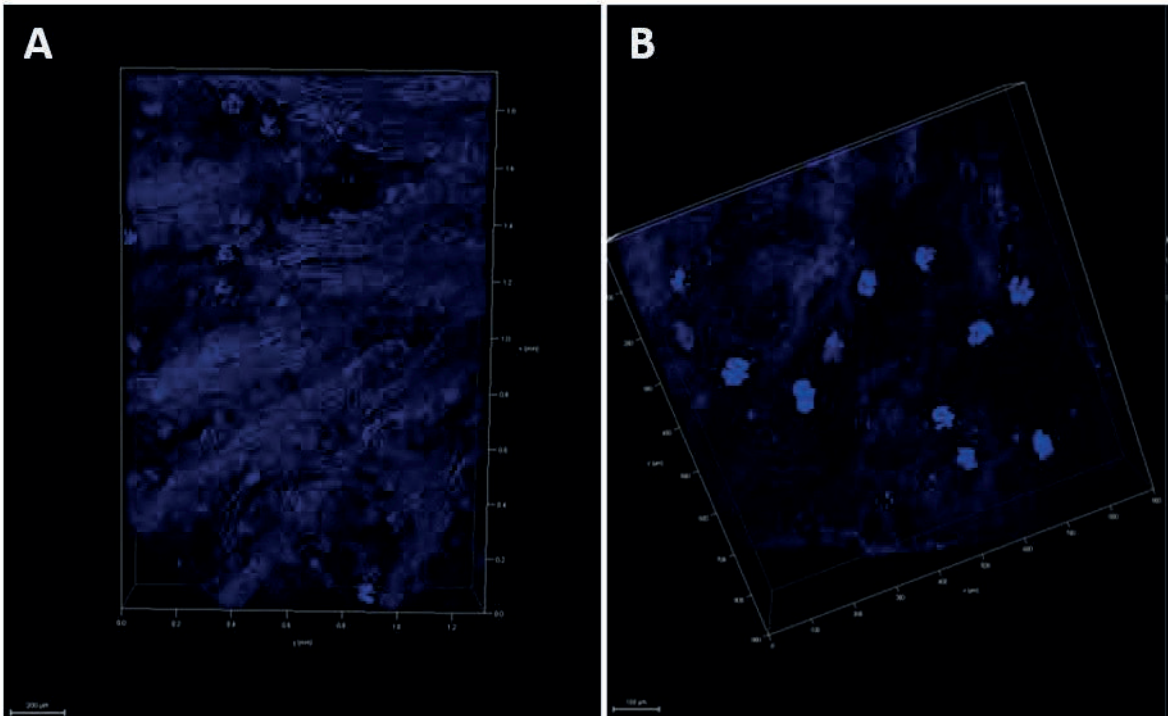

Figure 3.16 Sections of a mouse kidney (3D) acquired by CM using a 16x objective in immersion oil. Staining: podocin detected by Alexa Fluor 568 in 552 channel (blue); (A) with PFA post-fixation and (B) without PFA post-fixation. Scale bar: 200 µm

Due to the strong intrinsic autofluorescence of renal tissue, all the steps required for IHC were carefully examined. Making use of infrared and far-red fluorophore-conjugated secondary antibodies can give some advantages, but highly depends on the availability of suitable lasers that the imaging system provides. In our study, 3 lasers were available to excite the samples at 488, 552, and 638 nm respectively. Therefore, the selection of fluorophores was limited to Alexa Fluor 647 and Alexa Fluor 568/594. The latter fluorophore exhibited a slight overlap with the autofluorescence excitation range in the orange region of the spectrum. Overall, to minimize the background signal, the following criteria were considered for further protocol optimization:

1) Removal of unnecessarily prolonged fixation/post-fixation of the tissue
2) Addition of donkey serum to the immunofluorescence-staining buffers
3) Addition of anti-podocin and anti-CD31 in two separate steps (dual staining)

The preservation of a specific fluorescent signal against a low background, is particularly important for segmentation purposes. We measured the SNR in different ROIs (Figure 3.17) acquired from podocin stained sections. SNR significantly increased when the optimization criteria outlined above were applied.

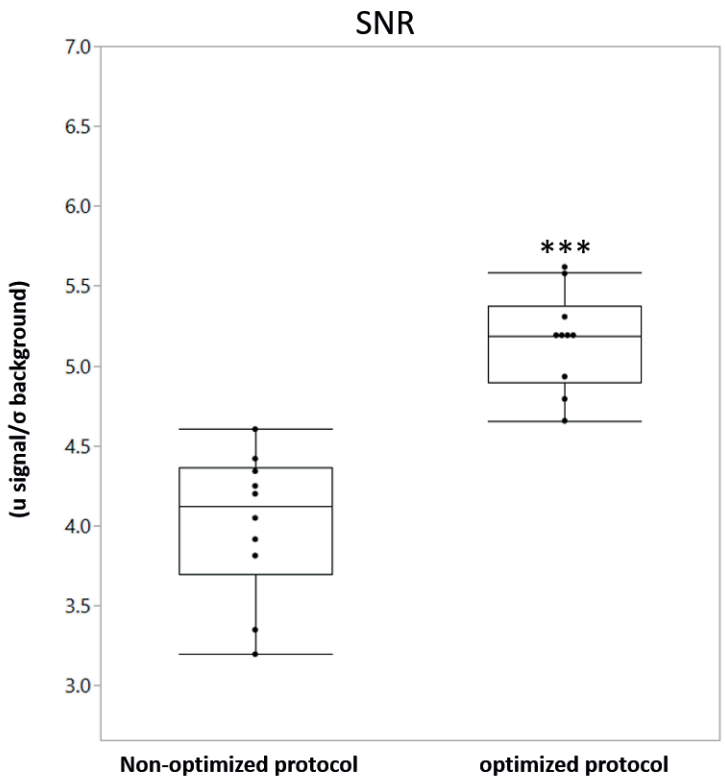

Figure 3.17 SNR calculated as the ratio of mean signal intensity in identified glomerular regions and the average mean signal intensity of background (μSIGNAL/σBACKGROUND). The measurements were obtained by calculating the SNR in non-optimized protocol (overfixation) and optimized protocol. The values are expressed as ratio. Asterisks indicate significance (***p < 0.001) in a t-test between the SNR related to the non-optimized and optimized protocol, error bars denote SD. The sample size is n = 10

3.2.3 Glomerular analysis in a preclinical model

Double staining of vessels and podocytes in mouse kidney can help to elucidate pathological mechanisms involved in the progression of renal disease. This strategy was combined with tissue clearing to investigate vascular defects in Has2 KO mice. Results from earlier studies demonstrated that the lack of HA from the endothelial glycocalyx leads to a loss of vessel stability in specific microcirculatory vascular beds[64, 73]. Kidneys were perfused and thereafter, 1 mm thick tissue sections were subjected to the optimized IHC-ECi clearing and imaged by CM.

In figure 3.18, an optical section representing the podocin channel (on the left) and autofluorescence channel (on the right) is shown.

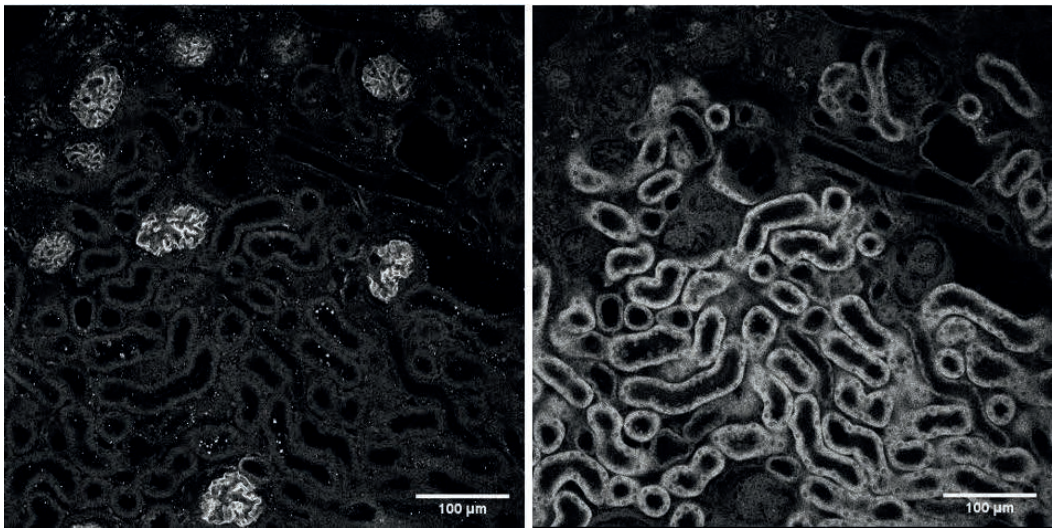

Figure 3.18 Section of mouse kidneys (2D, in gray scale) acquired by CM using a 20x objective in immersion oil. Staining: podocin detected by Alexa Fluor Plus 594 in 552 channel on the left; autofluorescence detection in 488 nm channel on the right. Scale bar: 100 µm

The glomerular analysis was performed to identify and quantify vascular defects by adopting a semi-automated approach as per the pipeline illustrated in figure 3.19.

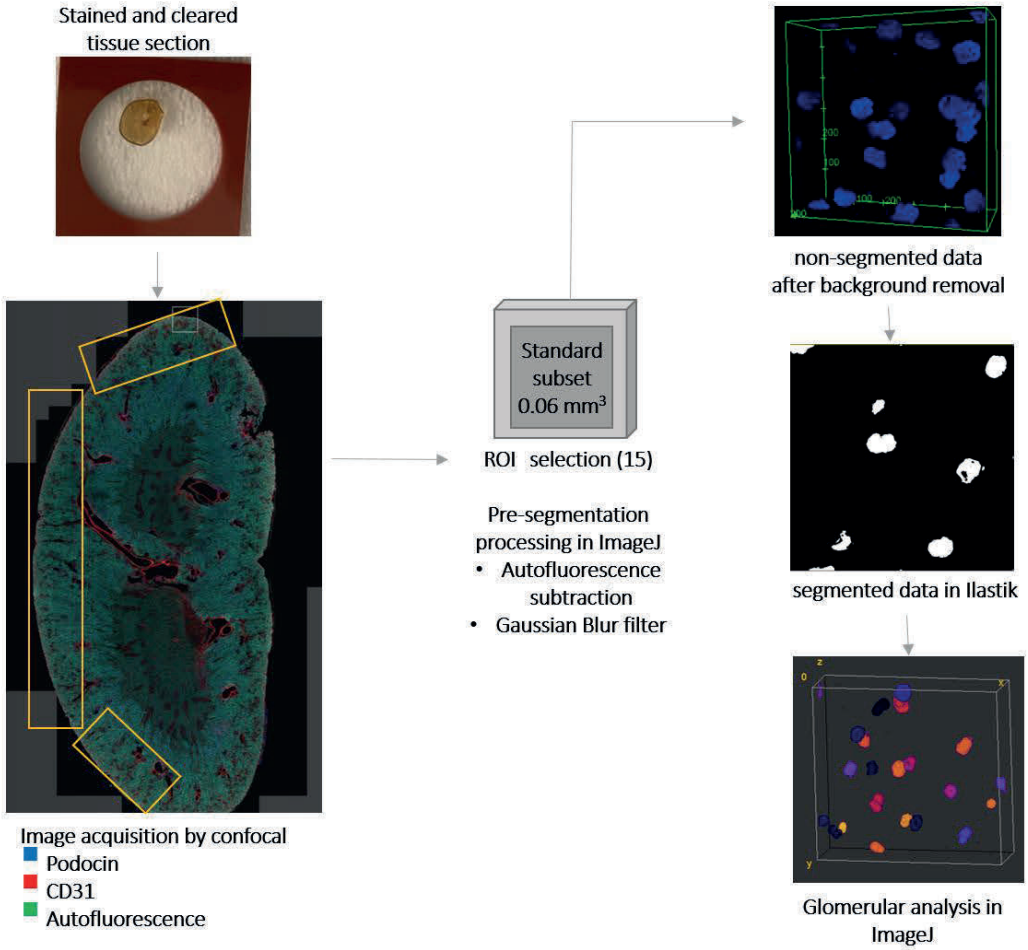

Figure 3.19 semi-automated pipeline for glomerular analysis: from image acquisition to glomerular segmentation

In 15 optical subsets corresponding to 0.9 mm^3 of the whole section, glomeruli were segmented. 3D imaging not only allowed counting of glomeruli within the optical section but also to estimate Feret's diameter in both the control- and Has2 group. Segmentation was performed by overlaying both the CD31 and the podocin channel in order to obtain the morphological information concerning the glomerular size in an accurate manner. This prevented exclusion of elements that were weakly labelled by NPHS2 (podocin). Despite the presence of multiple shrunk glomeruli in renal tissue collected from Has2 KO mice, there were no significant differences between in glomerular size distribution and number of glomeruli (data not shown). However, in Has2 KO mice kidneys, some structural changes in glomeruli could be observed when CD31 was selectively detected at higher magnification (some of these aberrations are indicated by yellow arrow in figure 3.20). Figure 3.20 A and B might be useful for qualitative assessment of vascular damage; quantification hereof did not reveal statistically significant differences.

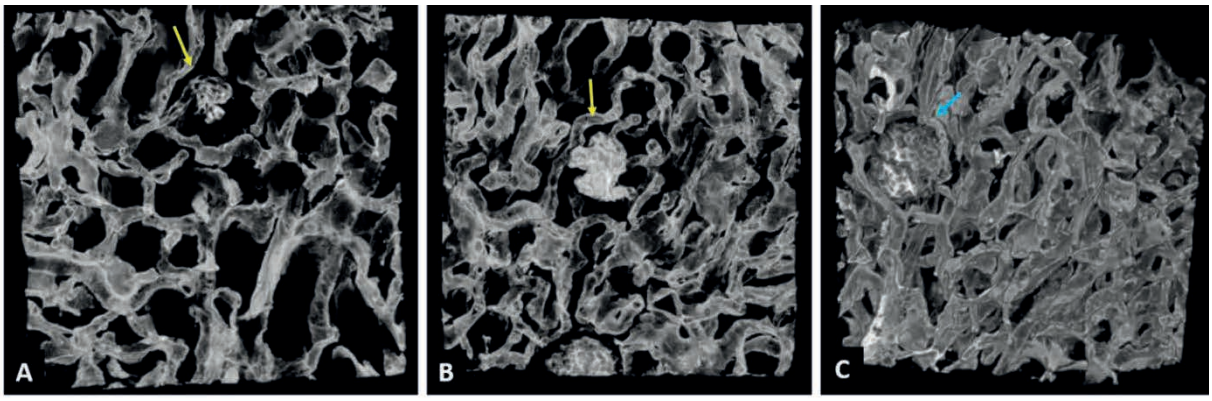

Figure 3.20 Sections of mouse kidney (3D) acquired by CM using a 40x objective in immersion oil. Staining: CD31 detected by Alexa fluor 647 in 638 channel. 3D reconstruction in ImageJ VolumeViewer. The yellow arrows in A and B show glomerular aberrations as compared to a normal glomerulus in C (blue arrow).

3.3 ExM optimization

Protocol optimization is based on principles that were examined previously[50]. The samples were processed according to three different protocols until optimal conditions were obtained to visualize podocytes without compromising fluorescence and tissue integrity. All protocols were performed as illustrated in figure 3.21.

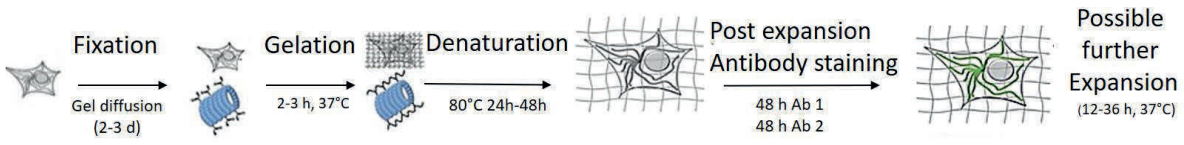

Figure 3.21 Schematic representation of the ExM steps for sample preparation adapted from Tilberg et al. [74].

3.3.1 Protocol optimization

Since the use of SA has been debated previously[67], the samples were embedded in a SA-free gel as a first approach. In addition, image acquisition was further improved by reducing the pinhole size and by employing green fluorophores for staining[75] (Figure 3.22).

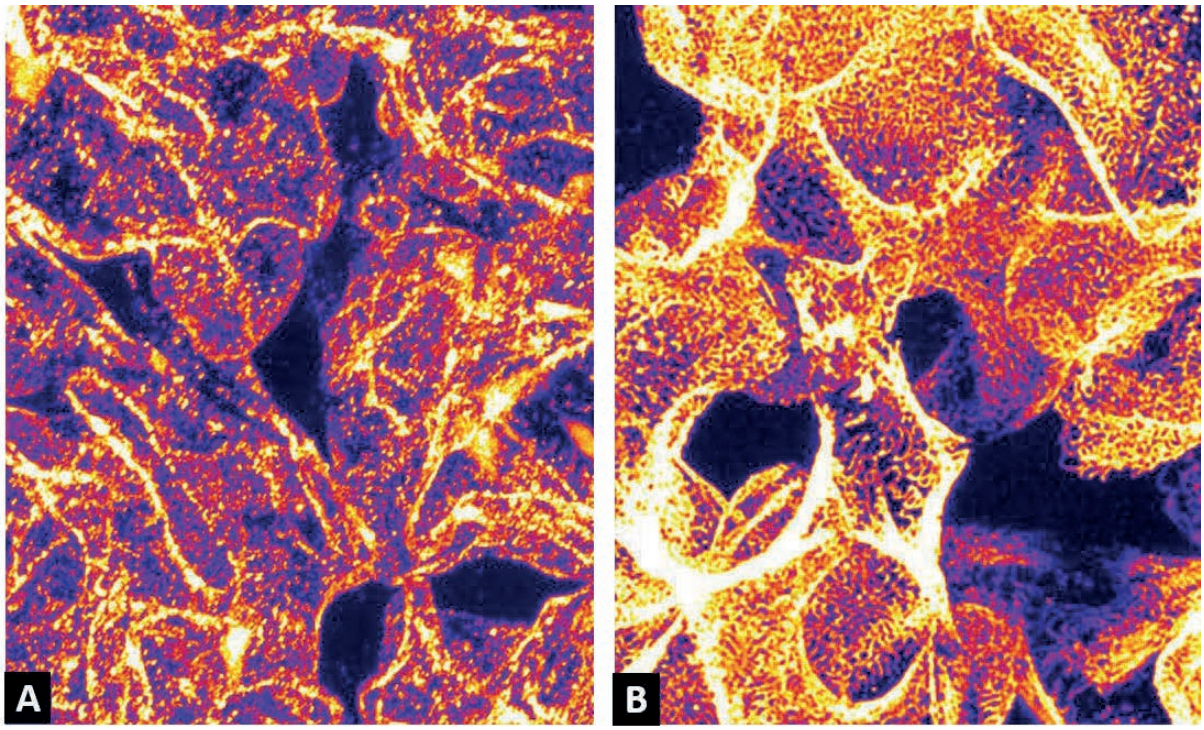

Figure 3.22 Comparison of imaging performance of samples embedded in AHS (A) or in SA-free (B) gels. Sections of mouse kidneys (represented as maximum projections) were imaged after expansion in water by CM using a 63x objective. Staining: podocin detected by Alexa Fluor 647 at 638 nm (A) and detected by STAR FLUOR 488 at 488 nm (B). A Fire LUT was applied using ImageJ in order to show differences in the fluorescence signal detection before optimization (A) and after optimization (B). The optimized protocol leads to preservation of tissue integrity at sub-molecular level and of fluorescence properties.

Nevertheless, some limitations common to ExM protocols persisted in specific tissues such as the loss of fluorescence and unsuccessful optical acquisition. As such, a decrease in fluorescence signal was observed specifically in rat tissue (figure 3.23 A). Also slight movement or vibration of the sample during the imaging posed an additional technical challenge as it caused focus-drift (Figure 3.23 B).

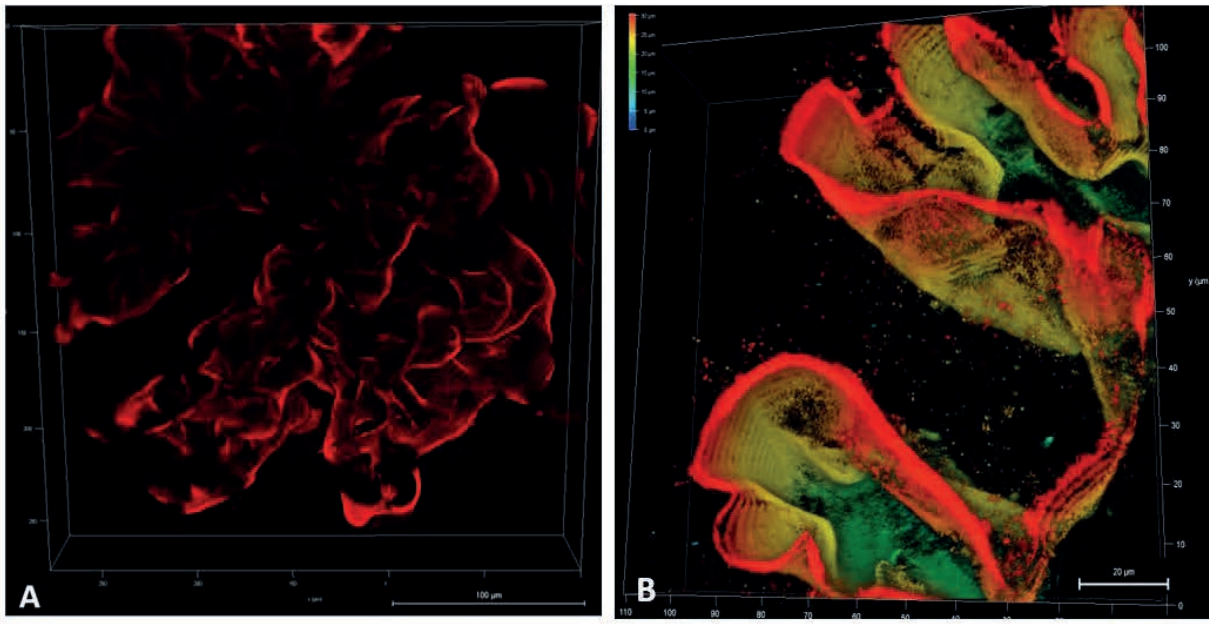

Figure 3.23 Sections of rat kidneys (3D) acquired by CM using a 63x objective in expansion water. Staining: podocin detected by STAR FLUOR 488 in 488 channel. A) Loss of autofluorescence in red, scale bar: 100 µm; B) focus drift in depth code, scale bar: 20 µm.

In order to address these drawbacks, the protocol was limited to two rounds of tissue denaturation when processing rat kidneys as the tissue already expands during the denaturation sufficiently enough to visualize fine structures. The subsequent higher stiffness resulted in a significantly improved quality of imaging (Figure 3.24).

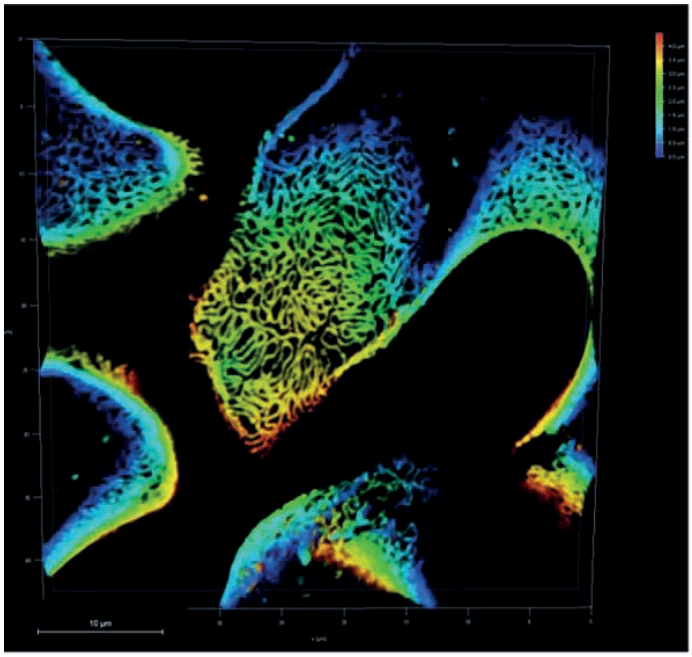

Figure 3.24 Section of a rat kidney (3D) acquired by CM using a 63x objective in expansion water, after denaturation for 48 hours Staining: podocin detected by STAR FLUOR 488 in 488 channel. The sample was fixed to the dish by agarose-embedding, to circumvent focus-drift. Color-coded image to improve depth perception from yellow (closer) to blue (further). scale bar: 10 µm

In parallel, mouse kidney sections were processed up to denaturation phase as well, in order to test the clearing efficacy of the protocol. In this case, the renal vascular

network was stained by CD31 as conducted for the IHC-ECi clearing protocol. In figure 3.25 the depth coded representation of renal vessels evidences the higher imaging depth that can be achieved by CM (≈1 mm) in gel-embedded and denaturated samples.

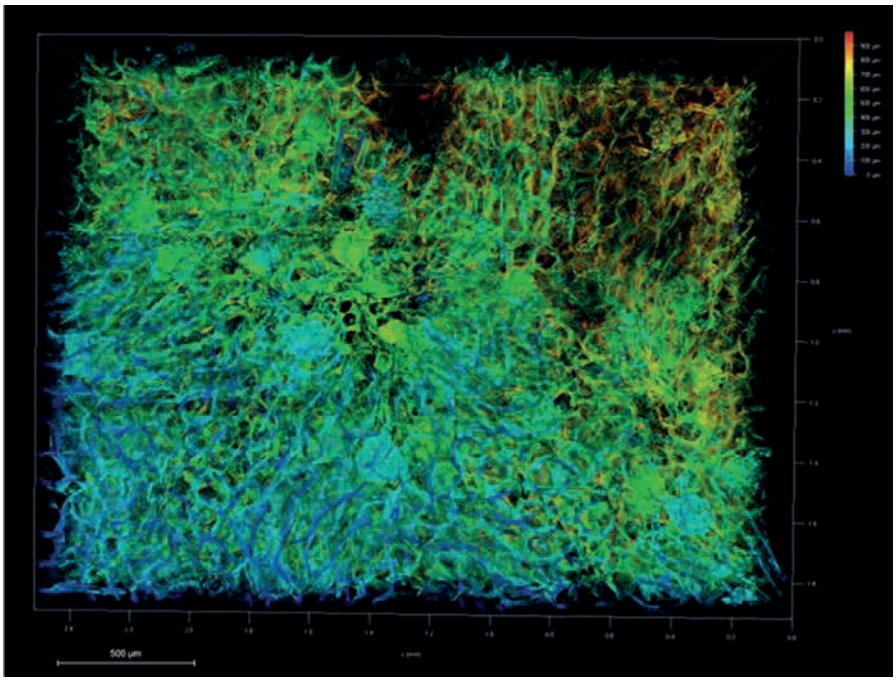

Figure 3.25 Sections of mouse kidney (3D) acquired by CM using a 16x objective in 1xPBS, after denaturation only Staining:CD31 detected by Alexa Fluor 647 in 638 channel. Color-coded image to improve depth perception from yellow (closer) to blue (further) Scale bar: 500µm

3.3.2 ExM factor calculation for comparison

The ExM factor measurements were calculated for assessing the expansion rate of the samples and comparing the performance of SA-free gels similar to ZOOM (protocol A) after increasing the concentration of NaCl and decreasing the concentration of Bisacrylamide in the gel composition (protocol B). Calculations of the expansion factor can be based on the sample enlargement by taking into account the ratio between the diameter of biological structures measured in the pre-expanded samples and in the expanded ones (i.e. linear expansion ratio). Other possibilities for calculating the expansion factor include a weight-based approach, i.e. a volumetric expansion factor obtained as weight-ratio of the expanded over the original sample or a linear expansion factor obtained as the ratio of the expanded diameter over the original diameter measured in the polymeric gel[76].

A more accurate alternative to measuring the expansion factor takes into consideration biological structures that expand in the sample. In our study, we selected the nuclear structures that are easily detected by nuclear staining (Sytox green) before and after

the expansion. For the nuclear diameter measurements, the raw data from figure 3.26 were segmented using the model Cyto in Cellpose. Objects on the edges or elements with sphericity lower than 0.7 were discarded to avoid artefacts. In figure 3.26 (A) and (C), a single Z-plane of the tissue section (mouse kidney) pre- and post-expansion is shown together with the corresponding segmented data 3.26 (B) and (D).

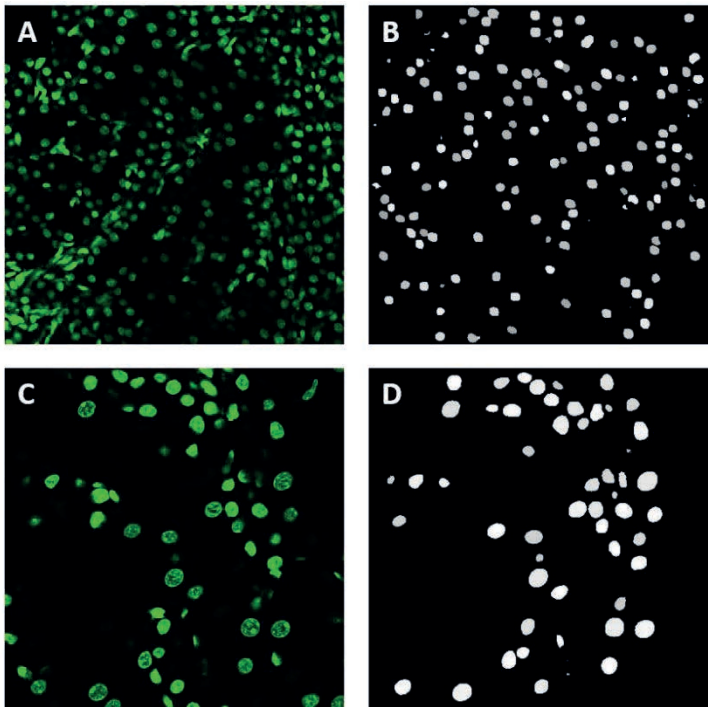

Figure 3.26 Nuclei in mouse kidney section imaged by CM, 16x objective in 1xPBS before denaturation (A) and in expansion water after denaturation and expansion (C). Staining: Sytox green in 488 channel (green). Segmented data as binary mask obtained in Cellpose before expansion (B) and after expansion (D).

The results of rat and mouse kidney tissue expansion were obtained by comparing 3 large regions (ROIs) of the sections following protocol A and B. As evidenced in figure 3.27, a significant increase of the nuclear diameter after the expansion was achieved for both the protocols.

Basing on the mean diameter of the nuclei, the differences between the linear expansion ratio in samples processed according to protocol A and B were not significantly different (see Figure 3.28).

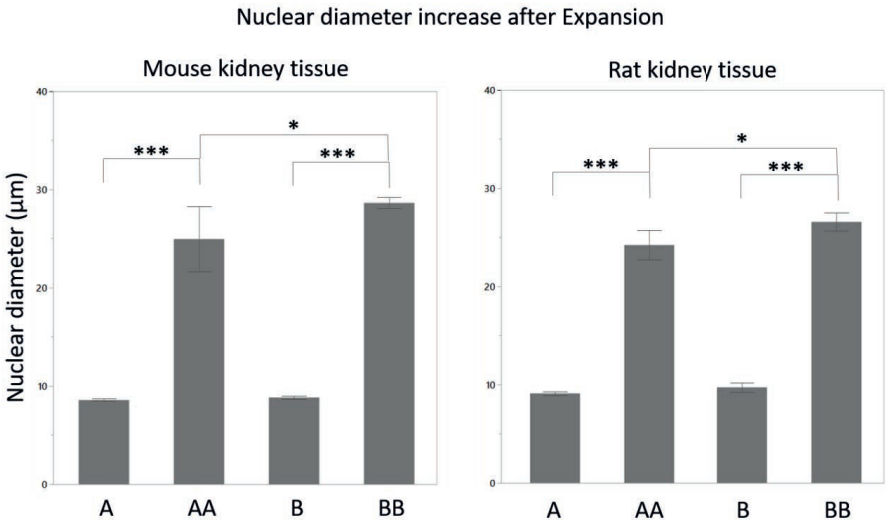

Figure 3.27 Nuclear diameter increase in mouse tissue (left) and rat tissue (right). The values are obtained by calculating the diameter in segmented nuclei (150 nuclei/ROI) in ROIs before (A and B) and after the expansion (AA and BB). Asterisks indicate significance *p < 0.05 and ***p < 0.001 in a t test (each pair) respectively between the expanded and not expanded (A vs. AA; B vs. BB) and between the expanded samples processed according protocol A and protocol B (AA vs. BB). Error bars denote SD. The sample size is n=3.

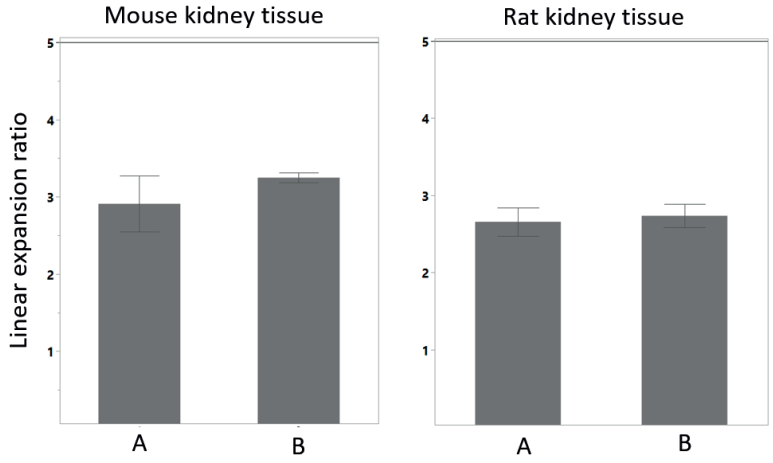

Figure 3.28 Linear expansion ratio in mouse tissue (left) and rat tissue (right). The values are the ratio between the mean diameter of expanded and not-expanded tissue processed according to protocol A and protocol B. Error bars denote SD. The sample size is n=3.

4 DISCUSSION

4.1 Strategies for optical imaging of renal vascular structures

With the introduction of OTC protocols, it has been possible to image large volumes and reconstruct biological structures three-dimensionally over the last decades. Morphological changes that can occur in different segments of the entire vasculature are important hallmarks in many pathophysiological conditions such as small vessel vasculitis[77], atherosclerosis[78], diabetic nephropathy[79], lupus nephritis[80], glomerulonephritis[81]. Therefore, new microscopy-based techniques have been recently introduced for visualization and analysis of vessels and capillaries[82]. Visualization of the vasculature can be obtained by organ/animal perfusion with dyes that selectively bind to the endothelium or glycocalyx, by making use of FP that is selectively expressed by endothelial cells, and by making use of antibodies against endothelial cell markers. In particular, the former strategy offers certain advantages as it stains the vasculature rapidly, making it a perfect candidate strategy for whole-organ imaging. Nonetheless, it should be underscored that most if not all dyes used for vascular imaging are not antigen-specific but bind to the vessel through electrostatic interactions between the dye and negatively or positively charged moieties of a multitude of different antigens. We explored an antigen-specific, i.e. antibody-based, approach for tracking the vasculature and the glomeruli in two separated imaging acquisition channels. To this end two different antibodies were used, one directed against endothelial cells and the other one directed against podocytes exclusively localised in glomeruli. Since the use of high concentrations of antibodies is expensive and IHC applied to large specimens can be very time-consuming, we only processed the tissue ex-vivo and worked on thick sections in lieu of large samples. This approach was particularly useful for targeting specific vascular structures and for more precisely segmenting glomeruli. It should be underlined that the selection of an appropriate optical instrument is also of crucial importance for vascular imaging and may vary depending on the complexity of the acquisition settings required for the imaging.

Large volume of renal tissue perfused with SV620C-01-PEI were imaged both by LSFM and CM throughout this project. As discussed in earlier studies, the use of NIR dyes and long-working distance dipping objectives for CM facilitates 3D imaging of thick specimens by increasing the light penetration depth and corresponding data acquisition. Nevertheless, as confocal microscopes illuminate the entire tissue

thickness when acquiring an optical Z-section from a single plane, they are more prone to bleaching fluorophores than light-sheet microscopes. Furthermore, despite the high photo-stability of SV620C-01-PEI, imaging of intact mouse kidneys by CM is challenging due to the slow acquisition time and the lower Z-resolution.

Depending on the parameters chosen for the acquisition, e.g. resolution, acquisition time can differ significantly between light-sheet and confocal (the acquisition time for similar resolution for LSFM vs. CM corresponds to 1 hour vs. 12 hours.). Therefore, the use of a light-sheet microscope is preferable, for the imaging of big-sized samples when capturing fine details is not needed, as shown in this work for the visualization of glomeruli in a large mouse kidney sample.

In this study, LSFM was adopted for a more extensive investigation on the clearing effectiveness of the IHC-ECi protocol allowing to make comparison at a higher acquisition depth. Due to instrumental limitations, the use of LSFM could not be extended to a wide range of specimens and also not to acquisitions that require a far-red laser and detection of a selective emission range. CM was therefore chosen for imaging of antibody-stained kidney sections requiring acquisition in more than 2 channels as well as for detection of far-red emitting fluorophores (SV770Z-01).

4.2 Fluorescent markers for vascular staining

Along with the implementation of dyes that can be used for organ perfusion or intravenous injection to label the vasculature, the search for molecules that fulfil this purpose and can be used in a cost-effective manner in combination with rapid tissue clearing protocols is gaining interest amongst scientist in academia and industry. The compounds tested in this work are conjugates of a fluorophore and a polymer that binds to biological structures through electrostatic interactions. As such, the PEI-conjugates and chitosan-conjugates can be used for perfusion through a rapid and easy staining procedure as compared to EB which is usually administrated up to 12 hours in advance[46, 83]. Both the PEI- and chitosan conjugates bind to the negatively charged glycocalyx of the vasculature. The replacement of MHI-148-PEI with the SV620C-01-PEI has overcome several disadvantages especially concerning the stability of the compound and the dose required for the administration. In the related comparative study, both MHI-I48 conjugate and corresponding mixture, label glomeruli in a similar manner while unconjugated SV620C-01 is only responsible for minor labelling. The residual staining is likely the result of the negatively charged glomerular basement membrane interacting with the unconjugated cationic dye that based on its

molecular weight would mostly freely pass the glomerular filtration barrier. In addition, in regard to the molecule MHI-148-PEI, chemical analysis disclosed batch-to-batch variation due to intermolecular electrostatic interactions between the MHI-148 and the PEI moieties. This explains why the glomerular endothelium is prevalently labelled by the non-covalently conjugated MHI-148 mixture, even though the molecular weight of the fluorophore is below the cut-off for glomerular filtration. Even though the SV620C-01-PEI conjugate was more stable and displayed a higher fluorescent intensity, the labelling efficacy of capillaries was low. Therefore, additional doses for the perfusion were tested. A dose lower than 1 mg/mL reduced the SNR and required higher laser power for signal acquisition. Indeed, a dose equivalent to 2 mg/mL increased the amount of cationic PEI conjugate for more effective labelling of capillaries, the down-side however was that the high emission peak of SV620C-01 also caused local overexposure of the image particularly for larger vessels and glomeruli. These findings led us to limit the working concentration of SV620C-01-PEI to 1 mg/mL, although the capillary network is not fully stained at this dose.

Since lectins have been reported to label capillaries[84], we combined SV620C-01-PEI with STAR FLUOR 645 conjugated to WGA in the perfusion solution. SV620C-01 and STAR FLUOR 645 are characterized by a different emission wavelength interval so the fluorescent signal could be detected in two separated channels for comparison. Furthermore, the fluorescent conjugates were tested at iso-absorbic concentrations translating to comparable concentrations of fluorescent dyes. The higher brightness of STAR FLUOR 645 and simultaneous imaging of the dyes by the same laser (at 638 nm) could explain the poor signal detection of SV620C-01 in this setting. Only the use of iso-fluorescent (equivalent emission peak) concentrations would provide reliable information as to whether complementary vascular structures were stained in the combination. This can be achieved by decreasing the administration dosage of the STAR FLUOR 645, with the inconvenience of decreasing the amount of WGA binding to the endothelial glycocalyx. In order to address these drawbacks and additional disadvantages of SV620C-01-PEI, e.g. cytotoxicity[85] and additional absorbance peak at 488 nm, we also tested a less expensive option, i.e. fluorophore conjugated to WS-chitosan. Two fluorophores were chosen for conjugation, i.e. SV680A-02 which emits in the NIR, and SV770Z-01 with emission spectra in the far-red region allowing potentially deeper image acquisition. The administration dose of the molecule was calculated by considering the emission intensity of the dye as well as the DOL of the

molecule so that positively charged groups can sufficiently bind the endothelium. The results show a similar performance for both the NIR and far-red emitting fluorophore and this can be explained by the limited depth that can be achieved by CM. While for the first time, the effectiveness of fluorescent chitosan in labelling vessels and capillaries ex-vivo was demonstrated, further comparative studies based on the use of a light-sheet microscope would be worthwhile for future experiments involving whole-organ, whole-organism, and in-vivo imaging experiments.

4.3 Dual staining by IHC-ECi

Using fluorescently labelled molecules to perfuse whole animals has several advantages over conventional immunostaining as discussed above. One of the objectives of our study was to provide an alternative protocol that combines ECi clearing with immunofluorescence, to selectively stain podocytes in glomeruli and the vasculature. To this aim, we optimized an established protocol for obtaining 3D morphological information from kidney samples in depth. The sample preparation was shortened and DISCO reagents were replaced with ECi for the clearing, avoiding further complications related to the sample handling because of the use of harmful substances. ECi clearing was previously successfully combined with IHC by Brenna et al.[65]. We compared the staining performance when the antibody staining was either done before (pre-clearing IHC) or after (post-clearing IHC) the ECi procedure.

This study suggests that pre-clearing immunostaining as established in the optimized protocol allows imaging up to 600 µm in depth by LSFM, while when ECi is only used as delipidation reagent according to the former protocol (post-clearing IHC), incubating rehydrated samples in other RI matching solution such as glycerol 88%, cannot achieve the same clearing outcomes. Once an optimized protocol was defined, we broadened its compatibility with dual staining for multiple channel acquisitions. Although the intrinsic autofluorescence of cleared tissue provides additional morphological information concerning the renal tubular structures, we observed that it contributes to background noise when the tissue is excited between 488 nm and 552 nm. Therefore, we identified some factors that can help reduce the background, leading us to the following considerations:

1) Prolonged tissue-storage in PFA 4% causes increased detection of the autofluorescence that makes it difficult to detect fluorophores such as Alexa Fluor 568 and Alexa Fluor 594. For this reason, our samples were collected and fixed in PFA only overnight prior to the transfer into PBS.

2) The use of a specific serum that matches the secondary antibody host species, can avoid the detection of non-specific signals in all the channels, especially given the prolonged incubation times required for 3D IHC.
3) Increasing the number of washing steps by incubating the two primary antibodies separately also improves the specific staining.
4) The use of new-generation fluorophores with improved brightness overcomes the overlap with the autofluorescence signal. Autofluorescence can still be acquired in an additional channel to eliminate further background by channel subtraction when processing the images.

In addition, our protocol implementation includes the establishment of a pipeline for the segmentation that involves post-acquisition image processing and the quantitative analysis of the objects of interest. Even though the deep learning-based approach has gained increasing popularity, we presented a semi-automated pipeline that makes use of open-source software and does not require programming skills.

4.4 Image analysis in pathological samples

Changes in glomerular number and glomerular size correlate with risk factors for kidney diseases[86]. In the past, these glomerular features were estimated by applying methods such as MRI and the dissector/fractionator stereology technique. The latter is a destructive technique[87], while MRI-based experiments require access to high-field strength MRI scanner and are conducted in-vivo, with the risk of undertaking complex regulatory procedures[88]. The rapid development of OTC and 3D imaging technologies, has offered new solutions for reliable morphometric analysis while preserving the tissue integrity[2]. In our study we selected representative sections of 1 mm thickness and quantified glomeruli by following a semi-automated pipeline for the analysis of renal tissue from Has2 mice. This approach benefits from the combination of OTC with high-resolution imaging performed by CM, overcoming the issues that arise when reconstructing large samples acquired by LSFM, such as “big data” handling and analysis. The amount of data obtained by imaging a thick renal section includes a representative number of glomeruli that were selected exclusively in the cortical area based on an automated and randomized approach. Moreover, collecting information from two channels (podocin staining and CD31 staining) ensures a reliable quantification of glomeruli throughout the section, independently of the podocin expression that can be lower due to possible pathological conditions[89]. A lower signal

detection, as would be for podocin under pathological conditions, can be responsible for an imprecise segmentation. Hence, utilising information from both channels, prevents segmentation errors. In fact, CD31 is a specific marker for endothelial cells and when used for labelling the renal tissue, can provide supplementary information concerning the glomerular tuft.

Endothelial deletion of Has2 in adult mice leads to substantial loss of the glycocalyx structure. In the kidney of such mice vascular destabilization is characterized by mesangiolysis, capillary ballooning, and albuminuria. This process develops over time into glomerular capillary rarefaction and glomerulosclerosis[64]. We studied vascular damage in Has2 KO mice kidneys 8 weeks post-gene deletion, a time-point at which disease manifestation is not extensive. Indeed, no significant differences in glomerular size distribution and the number of glomeruli (data not shown) between Has2 KO and wild type mice were found, albeit that a few vascular aberrations were found when analysing CD31 staining. Hence, CD31 staining in cleared tissue can help assess morphological changes qualitatively and can be used to elucidate the nature of vascular alterations in combination with other labelling methods. For instance, the partial staining observed in pcy mouse kidney, might not be the result of actual structural damage, but the consequence of a limited perfusion efficacy related to the pathological status. Thus, the employment of a CD31 staining-based protocol can help clarify the lack of vascular staining evidenced by the use of perfused fluorescent markers in future comparative studies.

4.5 ExM

The glomerular filtration barrier plays a major role in maintaining the kidney function[90]. Identifying new tools for assessing foot process effacement can yield new insights into the onset and progression of kidney diseases. For years, the ultrastructural analysis of renal biopsies at nanoscale level relied on electron microscopy. Recently, along with the introduction of new technologies such as SRM techniques, the development of ExM protocols made possible to resolve the renal nanostructures by means of accessible and low-cost microscopes. Over the last years, a multitude of ExM protocols have been developed with the purpose of achieving 3D high-resolution imaging and resolving the finest structures in biological tissue by physical expansion. To this aim, the samples are embedded in a cross-linked swellable polyelectrolyte hydrogel before or after the labelling. ExM involves digestion or denaturation of the tissue-gel hybrid that reduces sample inhomogeneity and makes it transparent. After this procedure, the

tissue is optically cleared and suitable for 3D imaging as shown in the result section. Although most of the protocols employ pre-expansion staining, labelling the tissue-gel hybrid in the final phase of the sample processing, allows re-using the tissue for multiplex immunofluorescence[91]. In this case, epitope preservation under denaturation conditions is critical. As shown in our study, denaturation in a SDS-based buffer at 80°C, does not affect CD31 and podocin staining in samples processed according to the optimized protocol.

Although we have shown that ExM helps achieve the desired high transparency for imaging samples in-depth, this method has been carried out throughout the project only to resolve fine renal structure, while ECi-based methods are preferential for simple OTC. Apart from the complex and time-consuming sample preparation, 3D microscopic examination of large expanded volumes might be cumbersome due to the sample stiffness and to the enormous datasets generated by the volumetric expansion. ExM is advantageous, howbeit, to study small details/structures in the sample that otherwise would only be visible by electron microscopy. We sought to visualize the podocyte's slit diaphragm and foot processes in renal tissue.

The protocol that we adapted makes use of a polymeric gel developed by Park et al., applied previously for analysing brain tissue. Eliminating SA in the gel recipe resulted in improved hydrogel stability in terms of polymerization and increased mechanical properties of the tissue-gel hybrid in renal tissue as well, in line with the findings reported in the former study[67].

Moreover, we investigated whether further modifications to the original protocol would improve the expansion rate. Although the change of NaCl and bisacrylamide concentrations were expected to influence the swelling pressure of the gel-tissue hybrid by increasing the gel osmotic pressure and decreasing the gel-crosslinking respectively[92], we did not observe a significant difference. The protocol optimization was mainly based on a trade-off of other factors such as tuning the denaturation time and improving the imaging acquisition settings as discussed in Unnersjo-Jess et al.[75]. Specifically, replacing red fluorophores with green fluorophores for the immunolabeling has led to substantial improvements as well as acquiring images with reduced pinhole size and decreased scan speed. In this way, it is possible to visualize the podocyte's slit diaphragms in rat kidney tissue without subjecting the samples to further expansion rounds. Moreover, with this approach, it was possible to address some drawbacks common in physically expanded biological specimens, such as loss of fluorescence

and focus drifting. The key strength of this technique applied in kidney research is the possibility of observing podocytes three-dimensionally. Anyway, future research is needed to investigate a reliable quantitative method for the evaluation of podocytes' morphometric parameters that are involved in pathophysiological processes.

5 SUMMARY

OTC techniques have been of ground-breaking importance for the 3D imaging of whole organs and whole-organism and have disclosed detailed information about intact biological systems at cellular and subcellular level. In several studies the use of OTC for visualization, mapping and quantification of tissue biopsies, has proven to be crucial for identifying pathological features. Since OTC protocols are often based on time-consuming and cumbersome procedures and require expensive or toxic reagents, there is a genuine need for further optimization. Moreover, the large amount of information deriving from 3D optical imaging demands a deep expertise for data handling and data analysis.

In this study, we optimized existing OTC techniques by focusing on the following major aspects: reduction of throughput time for sample preparation, implementation of staining strategies, improving of tissue handling, obtainment of suitable data for morphometric analysis of the kidney. By optimizing existing methods, we were able to visualize and analyse renal structures that play a key role in the kidney function such as peritubular capillaries, glomeruli and podocytes. Interestingly, by selecting new fluorescent biomarkers, we provide novel solutions to stain the whole renal vasculature as an alternative to expensive and time-consuming options. In addition, we replaced some shortcomings in previously described tissue clearing methods by faster and more easy-to-perform protocols. However, the future application of these techniques for the assessment of pathophysiological conditions will require additional optimisation in terms of microscope systems innovation and automated strategies for processing 3D data in order to accomplish a more accurate and less time consuming image acquisition and analysis. Yet, the optimization of clearing technologies that was carried out in this project offers novel insights on the application of these techniques in kidney research and opens new avenues for advancing the diagnostic field, by reducing the complexity of the currently available procedures.

6 REFERENCES

1. Tian, T, Yang, Z, Li, X: Tissue clearing technique: Recent progress and biomedical applications. *J Anat,* 238**:** 489-507, 2021. https://doi.org/10.1111/joa.13309
2. Puelles, VG, Combes, AN, Bertram, JF: Clearly imaging and quantifying the kidney in 3D. *Kidney Int,* 100**:** 780-786, 2021. https://doi.org/10.1016/j.kint.2021.04.042
3. Klingberg, A, Hasenberg, A, Ludwig-Portugall, I, Medyukhina, A, Mann, L, Brenzel, A, Engel, DR, Figge, MT, Kurts, C, Gunzer, M: Fully Automated Evaluation of Total Glomerular Number and Capillary Tuft Size in Nephritic Kidneys Using Lightsheet Microscopy. *J Am Soc Nephrol,* 28**:** 452-459, 2017. https://doi.org/10.1681/ASN.2016020232
4. Chen, F, Tillberg, PW, Boyden, ES: Optical imaging. Expansion microscopy. *Science,* 347**:** 543-548, 2015. https://doi.org/10.1126/science.1260088
5. Zhao, Y, Bucur, O, Irshad, H, Chen, F, Weins, A, Stancu, AL, Oh, EY, DiStasio, M, Torous, V, Glass, B, Stillman, IE, Schnitt, SJ, Beck, AH, Boyden, ES: Nanoscale imaging of clinical specimens using pathology-optimized expansion microscopy. *Nat Biotechnol,* 35**:** 757-764, 2017. https://doi.org/10.1038/nbt.3892
6. Richardson, DS, Lichtman, JW: Clarifying Tissue Clearing. *Cell,* 162**:** 246-257, 2015. https://doi.org/10.1016/j.cell.2015.06.067
7. Werner, S: Über das Durchsichtigmachen von menschlichen und tierischen Präparaten und seine theoretischen Bedingungen, nebst Anhang: Über Knochenfärbung. *S Hirzel*, 1914.
8. Costantini, I, Cicchi, R, Silvestri, L, Vanzi, F, Pavone, FS: In-vivo and ex-vivo optical clearing methods for biological tissues: review. *Biomed Opt Express,* 10**:** 5251-5267, 2019. https://doi.org/10.1364/BOE.10.005251
9. Yu, T, Zhu, J, Li, D, Zhu, D: Physical and chemical mechanisms of tissue optical clearing. *iScience,* 24**:** 102178, 2021. https://doi.org/10.1016/j.isci.2021.102178
10. Susaki, EA, Tainaka, K, Perrin, D, Kishino, F, Tawara, T, Watanabe, TM, Yokoyama, C, Onoe, H, Eguchi, M, Yamaguchi, S, Abe, T, Kiyonari, H, Shimizu, Y, Miyawaki, A, Yokota, H, Ueda, HR: Whole-brain imaging with single-cell resolution using chemical cocktails and computational analysis. *Cell,* 157**:** 726-739, 2014. https://doi.org/10.1016/j.cell.2014.03.042
11. Chung, K, Wallace, J, Kim, SY, Kalyanasundaram, S, Andalman, AS, Davidson, TJ, Mirzabekov, JJ, Zalocusky, KA, Mattis, J, Denisin, AK, Pak, S, Bernstein, H, Ramakrishnan, C, Grosenick, L, Gradinaru, V, Deisseroth, K: Structural and molecular interrogation of intact biological systems. *Nature,* 497**:** 332-337, 2013. https://doi.org/10.1038/nature12107
12. Brenna, C, Simioni, C, Varano, G, Conti, I, Costanzi, E, Melloni, M, Neri, LM: Optical tissue clearing associated with 3D imaging: application in preclinical and clinical studies. *Histochem Cell Biol,* 157**:** 497-511, 2022. https://doi.org/10.1007/s00418-022-02081-5
13. Tahaei, E, Coleman, R, Saritas, T, Ellison, DH, Welling, PA: Distal convoluted tubule sexual dimorphism revealed by advanced 3D imaging. *Am J Physiol Renal Physiol,* 319**:** F754-F764, 2020. https://doi.org/10.1152/ajprenal.00441.2020
14. Liu, H, Hiremath, C, Patterson, Q, Vora, S, Shang, Z, Jamieson, AR, Fiolka, R, Dean, KM, Dellinger, MT, Marciano, DK: Heterozygous Mutation of Vegfr3

Reduces Renal Lymphatics without Renal Dysfunction. *J Am Soc Nephrol,* 32**:** 3099-3113, 2021. https://doi.org/10.1681/ASN.2021010061

15. Wu, C, Yan, F, Li, M, Tu, Y, Guo, Z, Chen, Y, Wu, Y, Li, Q, Yu, C, Fu, Y, Wu, M, Kong, W, Gao, Y, Li, X, Zheng, J: Whole-Mount Kidney Clearing and Visualization Reveal Renal Sympathetic Hyperinnervation in Heart Failure Mice. *Front Physiol,* 12**:** 696286, 2021. https://doi.org/10.3389/fphys.2021.696286
16. Hasegawa, S, Susaki, EA, Tanaka, T, Komaba, H, Wada, T, Fukagawa, M, Ueda, HR, Nangaku, M: Comprehensive three-dimensional analysis (CUBIC-kidney) visualizes abnormal renal sympathetic nerves after ischemia/reperfusion injury. *Kidney Int,* 96**:** 129-138, 2019. https://doi.org/10.1016/j.kint.2019.02.011
17. Schuh, CD, Polesel, M, Platonova, E, Haenni, D, Gassama, A, Tokonami, N, Ghazi, S, Bugarski, M, Devuyst, O, Ziegler, U, Hall, AM: Combined Structural and Functional Imaging of the Kidney Reveals Major Axial Differences in Proximal Tubule Endocytosis. *J Am Soc Nephrol,* 29**:** 2696-2712, 2018. https://doi.org/10.1681/ASN.2018050522
18. Saritas, T, Puelles, VG, Su, XT, McCormick, JA, Welling, PA, Ellison, DH: Optical Clearing in the Kidney Reveals Potassium-Mediated Tubule Remodeling. *Cell Rep,* 25**:** 2668-2675 e2663, 2018. https://doi.org/10.1016/j.celrep.2018.11.021
19. Rodriguez-Nino, A, Pastene, DO, Hettler, SA, Qiu, J, Albrecht, T, Vajpayee, S, Perciaccante, R, Gretz, N, Bakker, SJL, Kramer, BK, Yard, BA, van den Born, J: Influence of carnosine and carnosinase-1 on diabetes-induced afferent arteriole vasodilation: implications for glomerular hemodynamics. *Am J Physiol Renal Physiol,* 323**:** F69-F80, 2022. https://doi.org/10.1152/ajprenal.00232.2021
20. Avilov, SV: Navigating across multi-dimensional space of tissue clearing parameters. *Methods Appl Fluoresc,* 9**:** 022001, 2021. https://doi.org/10.1088/2050-6120/abe6fb
21. Tainaka, K, Kubota, SI, Suyama, TQ, Susaki, EA, Perrin, D, Ukai-Tadenuma, M, Ukai, H, Ueda, HR: Whole-body imaging with single-cell resolution by tissue decolorization. *Cell,* 159**:** 911-924, 2014. https://doi.org/10.1016/j.cell.2014.10.034
22. Masselink, W, Reumann, D, Murawala, P, Pasierbek, P, Taniguchi, Y, Bonnay, F, Meixner, K, Knoblich, JA, Tanaka, EM: Broad applicability of a streamlined ethyl cinnamate-based clearing procedure. *Development,* 146, 2019. https://doi.org/10.1242/dev.166884
23. Molbay, M, Kolabas, ZI, Todorov, MI, Ohn, TL, Erturk, A: A guidebook for DISCO tissue clearing. *Mol Syst Biol,* 17**:** e9807, 2021. https://doi.org/10.15252/msb.20209807
24. Kirschnick, N, Drees, D, Redder, E, Erapaneedi, R, Pereira da Graca, A, Schafers, M, Jiang, X, Kiefer, F: Rapid methods for the evaluation of fluorescent reporters in tissue clearing and the segmentation of large vascular structures. *iScience,* 24**:** 102650, 2021. https://doi.org/10.1016/j.isci.2021.102650
25. Cai, R, Pan, C, Ghasemigharagoz, A, Todorov, MI, Forstera, B, Zhao, S, Bhatia, HS, Parra-Damas, A, Mrowka, L, Theodorou, D, Rempfler, M, Xavier, ALR, Kress, BT, Benakis, C, Steinke, H, Liebscher, S, Bechmann, I, Liesz, A, Menze, B, Kerschensteiner, M, Nedergaard, M, Erturk, A: Panoptic imaging of transparent mice reveals whole-body neuronal projections and skull-meninges connections. *Nat Neurosci,* 22**:** 317-327, 2019. https://doi.org/10.1038/s41593-018-0301-3
26. Kim, SY, Cho, JH, Murray, E, Bakh, N, Choi, H, Ohn, K, Ruelas, L, Hubbert, A, McCue, M, Vassallo, SL, Keller, PJ, Chung, K: Stochastic electrotransport

selectively enhances the transport of highly electromobile molecules. *Proc Natl Acad Sci U S A,* 112**:** E6274-6283, 2015. https://doi.org/10.1073/pnas.1510133112

27. Lee, E, Choi, J, Jo, Y, Kim, JY, Jang, YJ, Lee, HM, Kim, SY, Lee, HJ, Cho, K, Jung, N, Hur, EM, Jeong, SJ, Moon, C, Choe, Y, Rhyu, IJ, Kim, H, Sun, W: ACT-PRESTO: Rapid and consistent tissue clearing and labeling method for 3-dimensional (3D) imaging. *Sci Rep,* 6**:** 18631, 2016. https://doi.org/10.1038/srep18631
28. Kolesova, H, Olejnickova, V, Kvasilova, A, Gregorovicova, M, Sedmera, D: Tissue clearing and imaging methods for cardiovascular development. *iScience,* 24**:** 102387, 2021. https://doi.org/10.1016/j.isci.2021.102387
29. Shan, QH, Qin, XY, Zhou, N, Huang, C, Wang, Y, Chen, P, Zhou, JN: A method for ultrafast tissue clearing that preserves fluorescence for multimodal and longitudinal brain imaging. *BMC Biol,* 20**:** 77, 2022. https://doi.org/10.1186/s12915-022-01275-6
30. Kim, HJ, Kim, J, Choi, J, Sun, W: Chemical fluorescence-based dye staining for 3-dimensional histopathology analysis. *Anim Cells Syst (Seoul),* 26**:** 45-51, 2022. https://doi.org/10.1080/19768354.2022.2049641
31. Huang, J, Brenna, C, Khan, AUM, Daniele, C, Rudolf, R, Heuveline, V, Gretz, N: A cationic near infrared fluorescent agent and ethyl-cinnamate tissue clearing protocol for vascular staining and imaging. *Sci Rep,* 9**:** 521, 2019. https://doi.org/10.1038/s41598-018-36741-1
32. Zagorchev, L, Oses, P, Zhuang, ZW, Moodie, K, Mulligan-Kehoe, MJ, Simons, M, Couffinhal, T: Micro computed tomography for vascular exploration. *J Angiogenes Res,* 2**:** 7, 2010. https://doi.org/10.1186/2040-2384-2-7
33. Evans, RG, Eppel, GA, Anderson, WP, Denton, KM: Mechanisms underlying the differential control of blood flow in the renal medulla and cortex. *J Hypertens,* 22**:** 1439-1451, 2004. https://doi.org/10.1097/01.hjh.0000133744.85490.9d
34. Xue, S, Gong, H, Jiang, T, Luo, W, Meng, Y, Liu, Q, Chen, S, Li, A: Indian-ink perfusion based method for reconstructing continuous vascular networks in whole mouse brain. *PLoS One,* 9**:** e88067, 2014. https://doi.org/10.1371/journal.pone.0088067
35. Egawa, G, Nakamizo, S, Natsuaki, Y, Doi, H, Miyachi, Y, Kabashima, K: Intravital analysis of vascular permeability in mice using two-photon microscopy. *Sci Rep,* 3**:** 1932, 2013. https://doi.org/10.1038/srep01932
36. Miyawaki, T, Morikawa, S, Susaki, EA, Nakashima, A, Takeuchi, H, Yamaguchi, S, Ueda, HR, Ikegaya, Y: Visualization and molecular characterization of whole-brain vascular networks with capillary resolution. *Nat Commun,* 11**:** 1104, 2020. https://doi.org/10.1038/s41467-020-14786-z
37. Tsai, PS, Kaufhold, JP, Blinder, P, Friedman, B, Drew, PJ, Karten, HJ, Lyden, PD, Kleinfeld, D: Correlations of neuronal and microvascular densities in murine cortex revealed by direct counting and colocalization of nuclei and vessels. *J Neurosci,* 29**:** 14553-14570, 2009. https://doi.org/10.1523/JNEUROSCI.3287-09.2009
38. Li, Y, Song, Y, Zhao, L, Gaidosh, G, Laties, AM, Wen, R: Direct labeling and visualization of blood vessels with lipophilic carbocyanine dye DiI. *Nat Protoc,* 3**:** 1703-1708, 2008. https://doi.org/10.1038/nprot.2008.172
39. Konno, A, Matsumoto, N, Tomono, Y, Okazaki, S: Pathological application of carbocyanine dye-based multicolour imaging of vasculature and associated structures. *Sci Rep,* 10**:** 12613, 2020. https://doi.org/10.1038/s41598-020-69394-0

40. Ravnic, DJ, Jiang, X, Wolloscheck, T, Pratt, JP, Huss, H, Mentzer, SJ, Konerding, MA: Vessel painting of the microcirculation using fluorescent lipophilic tracers. *Microvasc Res,* 70**:** 90-96, 2005. https://doi.org/10.1016/j.mvr.2005.06.002
41. Jensen, KH, Berg, RW: CLARITY-compatible lipophilic dyes for electrode marking and neuronal tracing. *Sci Rep,* 6**:** 32674, 2016. https://doi.org/10.1038/srep32674
42. Konno, A, Matsumoto, N, Okazaki, S: Improved vessel painting with carbocyanine dye-liposome solution for visualisation of vasculature. *Sci Rep,* 7**:** 10089, 2017. https://doi.org/10.1038/s41598-017-09496-4
43. Honeycutt, SE, O'Brien, LL: Injection of Evans blue dye to fluorescently label and image intact vasculatur. *Biotechniques,* 70,3**:** 181-185, 2021. https://doi.org/10.2144/btn-2020-0152
44. Robertson, RT, Levine, ST, Haynes, SM, Gutierrez, P, Baratta, JL, Tan, Z, Longmuir, KJ: Use of labeled tomato lectin for imaging vasculature structures. *Histochem Cell Biol,* 143**:** 225-234, 2015. https://doi.org/10.1007/s00418-014-1301-3
45. Battistella, R, Kritsilis, M, Matuskova, H, Haswell, D, Cheng, AX, Meissner, A, Nedergaard, M, Lundgaard, I: Not All Lectins Are Equally Suitable for Labeling Rodent Vasculature. *Int J Mol Sci,* 22, 2021. https://doi.org/10.3390/ijms222111554
46. Todorov, MI, Paetzold, JC, Schoppe, O, Tetteh, G, Shit, S, Efremov, V, Todorov-Volgyi, K, During, M, Dichgans, M, Piraud, M, Menze, B, Erturk, A: Machine learning analysis of whole mouse brain vasculature. *Nat Methods,* 17**:** 442-449, 2020. https://doi.org/10.1038/s41592-020-0792-1
47. Matryba, P, Lukasiewicz, K, Pawlowska, M, Tomczuk, J, Golab, J: Can Developments in Tissue Optical Clearing Aid Super-Resolution Microscopy Imaging? *Int J Mol Sci,* 22, 2021. https://doi.org/10.3390/ijms22136730
48. Gao, R, Asano, SM, Upadhyayula, S, Pisarev, I, Milkie, DE, Liu, TL, Singh, V, Graves, A, Huynh, GH, Zhao, Y, Bogovic, J, Colonell, J, Ott, CM, Zugates, C, Tappan, S, Rodriguez, A, Mosaliganti, KR, Sheu, SH, Pasolli, HA, Pang, S, Xu, CS, Megason, SG, Hess, H, Lippincott-Schwartz, J, Hantman, A, Rubin, GM, Kirchhausen, T, Saalfeld, S, Aso, Y, Boyden, ES, Betzig, E: Cortical column and whole-brain imaging with molecular contrast and nanoscale resolution. *Science,* 363, 2019. https://doi.org/10.1126/science.aau8302
49. Unnersjo-Jess, D, Scott, L, Blom, H, Brismar, H: Super-resolution stimulated emission depletion imaging of slit diaphragm proteins in optically cleared kidney tissue. *Kidney Int,* 89**:** 243-247, 2016. https://doi.org/10.1038/ki.2015.308
50. Unnersjo-Jess, D, Scott, L, Sevilla, SZ, Patrakka, J, Blom, H, Brismar, H: Confocal super-resolution imaging of the glomerular filtration barrier enabled by tissue expansion. *Kidney Int,* 93**:** 1008-1013, 2018. https://doi.org/10.1016/j.kint.2017.09.019
51. Damstra, HGJ, Mohar, B, Eddison, M, Akhmanova, A, Kapitein, LC, Tillberg, PW: Visualizing cellular and tissue ultrastructure using Ten-fold Robust Expansion Microscopy (TREx). *Elife,* 11, 2022. https://doi.org/10.7554/eLife.73775
52. Chozinski, TJ, Mao, C, Halpern, AR, Pippin, JW, Shankland, SJ, Alpers, CE, Najafian, B, Vaughan, JC: Volumetric, Nanoscale Optical Imaging of Mouse and Human Kidney via Expansion Microscopy. *Sci Rep,* 8**:** 10396, 2018. https://doi.org/10.1038/s41598-018-28694-2
53. Siegerist, F, Endlich, K, Endlich, N: Novel Microscopic Techniques for Podocyte Research. *Front Endocrinol (Lausanne),* 9**:** 379, 2018. https://doi.org/10.3389/fendo.2018.00379

54. Gomez-Gaviro, MV, Sanderson, D, Ripoll, J, Desco, M: Biomedical Applications of Tissue Clearing and Three-Dimensional Imaging in Health and Disease. *iScience,* 23**:** 101432, 2020. https://doi.org/10.1016/j.isci.2020.101432
55. Ueda, HR, Erturk, A, Chung, K, Gradinaru, V, Chedotal, A, Tomancak, P, Keller, PJ: Tissue clearing and its applications in neuroscience. *Nat Rev Neurosci,* 21**:** 61-79, 2020. https://doi.org/10.1038/s41583-019-0250-1
56. Planchon, TA, Gao, L, Milkie, DE, Davidson, MW, Galbraith, JA, Galbraith, CG, Betzig, E: Rapid three-dimensional isotropic imaging of living cells using Bessel beam plane illumination. *Nat Methods,* 8**:** 417-423, 2011. https://doi.org/10.1038/nmeth.1586
57. Swoger, J, Verveer, P, Greger, K, Huisken, J, Stelzer, EHK: Multi-view image fusion improves resolution in three-dimensional microscopy *Optics Express,* 15**:** 8029-8042, 2007. https://doi.org/10.1364/OE.15.008029
58. Pietzsch, T, Saalfeld, S, Preibisch, S, Tomancak, P: BigDataViewer: visualization and processing for large image data sets. *Nat Methods,* 12**:** 481-483, 2015. https://doi.org/10.1038/nmeth.3392
59. Horl, D, Rojas Rusak, F, Preusser, F, Tillberg, P, Randel, N, Chhetri, RK, Cardona, A, Keller, PJ, Harz, H, Leonhardt, H, Treier, M, Preibisch, S: BigStitcher: reconstructing high-resolution image datasets of cleared and expanded samples. *Nat Methods,* 16**:** 870-874, 2019. https://doi.org/10.1038/s41592-019-0501-0
60. Vieites-Prado, A, Renier, N: Tissue clearing and 3D imaging in developmental biology. *Development,* 148, 2021. https://doi.org/10.1242/dev.199369
61. Berg, S, Kutra, D, Kroeger, T, Straehle, CN, Kausler, BX, Haubold, C, Schiegg, M, Ales, J, Beier, T, Rudy, M, Eren, K, Cervantes, JI, Xu, B, Beuttenmueller, F, Wolny, A, Zhang, C, Koethe, U, Hamprecht, FA, Kreshuk, A: ilastik: interactive machine learning for (bio)image analysis. *Nat Methods,* 16**:** 1226-1232, 2019. https://doi.org/10.1038/s41592-019-0582-9
62. Hallou, A, Yevick, HG, Dumitrascu, B, Uhlmann, V: Deep learning for bioimage analysis in developmental biology. *Development,* 148, 2021. https://doi.org/10.1242/dev.199616
63. Jiang, L, Chen, W, Dong, B, Mei, K, Zhu, C, Liu, J, Cai, M, Yan, Y, Wang, G, Zuo, L, Shi, H: A Deep Learning-Based Approach for Glomeruli Instance Segmentation from Multistained Renal Biopsy Pathologic Images. *Am J Pathol,* 191**:** 1431-1441, 2021. https://doi.org/10.1016/j.ajpath.2021.05.004
64. van den Berg, BM, Wang, G, Boels, MGS, Avramut, MC, Jansen, E, Sol, W, Lebrin, F, van Zonneveld, AJ, de Koning, EJP, Vink, H, Grone, HJ, Carmeliet, P, van der Vlag, J, Rabelink, TJ: Glomerular Function and Structural Integrity Depend on Hyaluronan Synthesis by Glomerular Endothelium. *J Am Soc Nephrol,* 30**:** 1886-1897, 2019. https://doi.org/10.1681/ASN.2019020192
65. Brenna, C, Khan, AUM, Picascia, T, Sun, Q, Heuveline, V, Gretz, N: New technical approaches for 3D morphological imaging and quantification of measurements. *Anat Rec (Hoboken),* 303**:** 2702-2715, 2020. https://doi.org/10.1002/ar.24463
66. Sun, Q, Picascia, T, Khan, AuM, Brenna, C, Heuveline, V, Schmaus, A, Sleeman, JP, Gretz, N: Application of ethyl cinnamate based optical tissue clearing and expansion microscopy combined with retrograde perfusion for 3D lung imaging. *Experimental Lung Research,* 46**:** 393-408, 2020. https://doi.org/10.1080/01902148.2020.1829183
67. Park, HE, Choi, D, Park, JS, Sim, C, Park, S, Kang, S, Yim, H, Lee, M, Kim, J, Pac, J, Rhee, K, Lee, J, Lee, Y, Lee, Y, Kim, SY: Scalable and Isotropic Expansion

of Tissues with Simply Tunable Expansion Ratio. *Adv Sci (Weinh),* 6**:** 1901673, 2019. https://doi.org/10.1002/advs.201901673

68. Wang, W, Meng, Q, Li, Q, Liu, J, Zhou, M, Jin, Z, Zhao, K: Chitosan Derivatives and Their Application in Biomedicine. *Int J Mol Sci,* 21, 2020. https://doi.org/10.3390/ijms21020487
69. Ollion, J, Cochennec, J, Loll, F, Escude, C, Boudier, T: TANGO: a generic tool for high-throughput 3D image analysis for studying nuclear organization. *Bioinformatics,* 29**:** 1840-1841, 2013. https://doi.org/10.1093/bioinformatics/btt276
70. Stringer, C, Wang, T, Michaelos, M, Pachitariu, M: Cellpose: a generalist algorithm for cellular segmentation. *Nat Methods,* 18**:** 100-106, 2021. https://doi.org/10.1038/s41592-020-01018-x
71. Nurnberg, E, Vitacolonna, M, Klicks, J, von Molitor, E, Cesetti, T, Keller, F, Bruch, R, Ertongur-Fauth, T, Riedel, K, Scholz, P, Lau, T, Schneider, R, Meier, J, Hafner, M, Rudolf, R: Routine Optical Clearing of 3D-Cell Cultures: Simplicity Forward. *Front Mol Biosci,* 7**:** 20, 2020. https://doi.org/10.3389/fmolb.2020.00020
72. Renier, N, Wu, Z, Simon, DJ, Yang, J, Ariel, P, Tessier-Lavigne, M: iDISCO: a simple, rapid method to immunolabel large tissue samples for volume imaging. *Cell,* 159**:** 896-910, 2014. https://doi.org/10.1016/j.cell.2014.10.010
73. Wang, G, de Vries, MR, Sol, W, van Oeveren-Rietdijk, AM, de Boer, HC, van Zonneveld, AJ, Quax, PHA, Rabelink, TJ, van den Berg, BM: Loss of Endothelial Glycocalyx Hyaluronan Impairs Endothelial Stability and Adaptive Vascular Remodeling After Arterial Ischemia. *Cells,* 9, 2020. https://doi.org/10.3390/cells9040824
74. Tillberg, PW, Chen, F, Piatkevich, KD, Zhao, Y, Yu, CC, English, BP, Gao, L, Martorell, A, Suk, HJ, Yoshida, F, DeGennaro, EM, Roossien, DH, Gong, G, Seneviratne, U, Tannenbaum, SR, Desimone, R, Cai, D, Boyden, ES: Protein-retention expansion microscopy of cells and tissues labeled using standard fluorescent proteins and antibodies. *Nat Biotechnol,* 34**:** 987-992, 2016. https://doi.org/10.1038/nbt.3625
75. Unnersjo-Jess, D, Butt, L, Hohne, M, Witasp, A, Kuhne, L, Hoyer, PF, Patrakka, J, Brinkkotter, PT, Wernerson, A, Schermer, B, Benzing, T, Scott, L, Brismar, H, Blom, H: A fast and simple clearing and swelling protocol for 3D in-situ imaging of the kidney across scales. *Kidney Int,* 99**:** 1010-1020, 2021. https://doi.org/10.1016/j.kint.2020.10.039
76. Cipriano, BH, Banik, SJ, Sharma, R, Rumore, D, Hwang, W, Briber, RM, Raghavan, SR: Superabsorbent Hydrogels That Are Robust and Highly Stretchable. *Macromolecules,* 47**:** 4445-4452, 2014. https://doi.org/10.1021/ma500882n
77. Maritati, F, Iannuzzella, F, Pavia, MP, Pasquali, S, Vaglio, A: Kidney involvement in medium- and large-vessel vasculitis. *J Nephrol,* 29**:** 495-505, 2016. https://doi.org/10.1007/s40620-016-0303-8
78. Klomjit, N, Zhu, XY, Eirin, A, Pawar, AS, Conley, SM, Puranik, AS, Ferguson, CM, Kim, SR, Tang, H, Jordan, KL, Saadiq, IM, Lerman, A, Grande, JP, Textor, SC, Lerman, LO: Microvascular remodeling and altered angiogenic signaling in human kidneys distal to occlusive atherosclerotic renal artery stenosis. *Nephrol Dial Transplant,* 37**:** 1844-1856, 2022. https://doi.org/10.1093/ndt/gfac156
79. Kida, Y: Peritubular Capillary Rarefaction: An Underappreciated Regulator of CKD Progression. *Int J Mol Sci,* 21, 2020. https://doi.org/10.3390/ijms21218255

80. Ding, Y, Tan, Y, Qu, Z, Yu, F: Renal microvascular lesions in lupus nephritis. *Ren Fail,* 42**:** 19-29, 2020. https://doi.org/10.1080/0886022X.2019.1702057
81. Ohashi, R, Kitamura, H, Yamanaka, N: Peritubular Capillary Injury during the Progression of Experimental Glomerulonephritis in Rats. *Cells,* 10,5 1087, 2021.
82. Zhu, J, Liu, X, Deng, Y, Li, D, Yu, T, Zhu, D: Tissue optical clearing for 3D visualization of vascular networks: A review. *Vascul Pharmacol,* 141**:** 106905, 2021. https://doi.org/10.1016/j.vph.2021.106905
83. Manaenko, A, Chen, H, Kammer, J, Zhang, JH, Tang, J: Comparison Evans Blue injection routes: Intravenous versus intraperitoneal, for measurement of blood-brain barrier in a mice hemorrhage model. *J Neurosci Methods,* 195**:** 206-210, 2011. https://doi.org/10.1016/j.jneumeth.2010.12.013
84. Kataoka, H, Ushiyama, A, Kawakami, H, Akimoto, Y, Matsubara, S, Iijima, T: Fluorescent imaging of endothelial glycocalyx layer with wheat germ agglutinin using intravital microscopy. *Microsc Res Tech,* 79**:** 31-37, 2016. https://doi.org/10.1002/jemt.22602
85. Kafil, V, Yadollah, O: Cytotoxic impacts of linear and branched polyethylenimine nanostructures in a431 cells.". *BioImpacts,* BI vol. 1,1 23-30, 2011.
86. Puelles, VG, Hoy, WE, Hughson, MD, Diouf, B, Douglas-Denton, RN, Bertram, JF: Glomerular number and size variability and risk for kidney disease. *Curr Opin Nephrol Hypertens,* 20**:** 7-15, 2011. https://doi.org/10.1097/MNH.0b013e3283410a7d
87. Beeman, SC, Zhang, M, Gubhaju, L, Wu, T, Bertram, JF, Frakes, DH, Cherry, BR, Bennett, KM: Measuring glomerular number and size in perfused kidneys using MRI. *Am J Physiol Renal Physiol,* 300**:** F1454-1457, 2011. https://doi.org/10.1152/ajprenal.00044.2011
88. Puelles, VG, Bertram, JF: Counting glomeruli and podocytes: rationale and methodologies. *Curr Opin Nephrol Hypertens,* 24**:** 224-230, 2015. https://doi.org/10.1097/MNH.0000000000000121
89. Pereira, LHM, da Silva, CA, Monteiro, M, Araujo, LS, Rocha, LP, Reis, M, Ramalho, FS, Correa, RRM, Silva, MV, Reis, MA, Machado, JR: Podocin and uPAR are good biomarkers in cases of Focal and segmental glomerulosclerosis in pediatric renal biopsies. *PLoS One,* 14**:** e0217569, 2019. https://doi.org/10.1371/journal.pone.0217569
90. Ehtesham, A, Deepak, N: Glomerular Filtration Barrier Assembly: An insight. *Postdoc Journal,* 1(4)**:** 33-45, 2013. https://doi.org/10.14304/SURYA.JPR.V1N4.4
91. Gallagher, BR, Zhao, Y: Expansion microscopy: A powerful nanoscale imaging tool for neuroscientists. *Neurobiol Dis,* 154**:** 105362, 2021. https://doi.org/10.1016/j.nbd.2021.105362
92. Hu, Y, Chu, X, Chen, TT, Pan, Q, Liu, C, Yi, J, Chu, X: Improving resolving ability of expansion microscopy by varying crosslinker concentration. *Chem Commun (Camb),* 56**:** 4176-4179, 2020. https://doi.org/10.1039/d0cc00052c

7 CURRICULUM VITAE AND PUBLICATIONS

PERSONALIEN

Name:	Picascia Tiziana
Date of birth:	4th November 1993
Place of birth:	Neapel, Italy
Nationality	Italian

EDUCATION

2019 – current	Ph.D Candidate in Experimental Medicine/Biotechnology ZMF, Mannheim University Hospital, University of Heidelberg
2012 – 2018	Master's Degree in Medicinal Chemistry and Pharmaceutical Technology Faculty of Pharmacy, University of Naples "Federico II" (Italy) Master's Thesis title: "Adenosine signaling mediates the anti-inflammatory effects of Nimesulide"

WORK EXPERIENCE

Apr 2023 – Present	Payload Integration Management Support Telespazio Belgium Srl - European Space Agency Topic: supporting the integration of scientific projects and coordinating with multidisciplinary teams for the execution of experimental activities aboard the ISS
Mar 2019 – Feb 2023	Early stage Researcher-Marie Skłodowska-Curie Actions ZMF, Mannheim University Hospital, University of Heidelberg Topic: Development and optimization of OTC and microscopy technologies for analysing organs and biopsies ex-vivo
Sept 2018 – Mar 2019	Post-graduate apprenticeship in Neuroscience School of Medicine, University of Naples "Federico II" (Italy) Topic: Focus on hypoxic-ischemic brain injury
Sept 2016 – Mar 2018	Master's Degree Internship in Pharmacology Faculty of Pharmacy, University of Naples "Federico II" (Italy) Topic: focus on in-vivo model of inflammation

RESEARCH ACTIVITY

PUBLICATIONS

1) Application of ethyl cinnamate based optical tissue clearing and expansion microscopy combined with retrograde perfusion for 3D lung imaging
Sun Q, **Picascia T**, Khan AUM, Brenna C, Heuveline V, Schmaus A, Sleeman JP, Gretz N. Exp Lung Res. 2020 Oct; 12:1-16.
doi: 10.1080/01902148.2020.1829183

2) Brenna C, Khan AUM, **Picascia T**, Sun Q, Heuveline V, Gretz N. technical approaches for 3D morphological imaging and quantification of measurements. Anat Rec (Hoboken). 2020 Oct;303(10):2702-2715New
doi: 10.1002/ar.24463

3) Mohammed M Yusuf, Vajpayee S, **Picascia T**, Perciaccante R, Gretz N. An overview of non-invasive methods for transcutaneous measurements of glomerular filtration. J Exp Nephrol 2021; 2(1):7-14.
doi:10.46439/nephrology.2.008

4) Sun Q, **Picascia T**, Khan AUM, Heuveline V, Gretz N. A simple optical tissue clearing pipeline for 3D vasculature imaging of the mediastinal organs in mice. Int J Exp Pathol. 2021 Aug;102(4-5):218-227.
doi: 10.1111/iep.12399

5) Hettler S A, **Picascia T**, Pastene D O, Vajpayee S, Perciaccante R, Yard B A, Gretz N, Krämer B K. Hyperfiltration can be detected by transcutaneous assessment of glomerular filtration rate (tGFR) in diabetic obese mice. Am J Physiol Cell Physiol. 2023 Nov (Online ahead of print)
doi:10.1152/ajpcell.00483.2022

POSTER PRESENTATION

1) **Picascia T**, Khan AM, Heuveline V, Gretz N. Optimization of optical tissue clearing methods for the morphological imaging of renal vascular structures.
Presented at RenalToolBox International Conference and Network Meeting in Liverpool (April 2022)

PATENT

1) Perciaccante R, Jansen TP, Vajpayee S, **Picascia T**, Gretz N. Fluorescent water-soluble polycationic chitosan polymers as markers for biological 3D imaging. Italian Patent Application No. 102022000022113.2022.

8 ACKNOWLEDGEMENTS

First of all, I would like to express my sincere gratitude to my former supervisor, Prof. Norbert Gretz for his mentorship, continuous trust and worthful advice throughout the project. A special thanks to Professor Benito Yard for contributing to the project with valuable insights in multiple phases of my research work and particularly for his supervision in finalising this manuscript at its latest stage. I would like to sincerely thank the Marie Skłodowska-Curie Innovative Training Network under the name 'RenalToolBox' that has offered me the extraordinary opportunity to collaborate with numerous researchers all over Europe with a special mention to Prof. Karen Bieback for her support in the frame of this international and multidisciplinary PhD program. I am especially grateful for the fruitful cooperation with our industrial partners, Cyanagen Srl including Dr. Rossana Perciaccante and Srishti Vajpayee, as well as Leica Microsystem which has provided access to cutting-edge imaging-based technologies employed in this work. Also, from RenalToolBox, I would like to thank Katerina Stripling and Prof. Bernard M. van den Berg for supplying the Has2 KO mice samples and providing extensive feedback on the results. My acknowledgment extends to the other ESRs I have closely worked with, for their collaborative attitude: Mohammed Yusuf, Alejandra Hernández-Pichardo and Eleonora Scaccia.

Moreover, I wish to show my appreciation to my colleague at UMM:

Dr. Diego Pastene, Dr. Arif ul Maula Khan and Dr. Cinzia Brenna for their remarkable expertise respectively in high-end microscopy, image analysis and tissue clearing;

Camela Jost, Viktoria Skude, Maria Muciek, Ina Schäfer, Elizabeth Wühl and Alexander Schlund for providing their technical knowledge and incessant help to the experimental activities along with a friendly mind-set;

Sina and Edda who helped me to navigate the German bureaucracy processes at the beginning of my PhD journey.

My deepest gratitude goes to my family and friends: to my parents who have always believed in me during this challenging path of professional and personal growth, beyond time and distance; to my best friend Gabriella and my friend Marco for their constant encouragement to pursue my ambitions; finally, to the friends who I met in Germany and despite all the odds, made Mannheim feel like home: Aparna, Kaushik, Nidhi and particularly Anca, whose relentless support has brought cheerfulness and motivation to succeed in every single day of this long journey.